Università degli Studi di Milano

GRADUATE SCHOOL OF VETERINARY SCIENCES

FOR ANIMAL HEALTH AND FOOD SAFETY

Director: Prof. Valentino Bontempo

Doctoral Program in Veterinary Clinical Sciences

Academic Year: 2011-2012

Multimodal Imaging in Oncology Research: Magnetic Resonance Imaging and Bioluminescence Studies in a Murine Model of Pancreatic Cancer

Micaela Russo

Tutor:

Prof. Mauro Di Giancamillo

Coordinator:

Prof. Fausto Cremonesi

Index

INTRODUCTION

1 INTRODUCTION

Pancreatic ductal adenocarcinoma (PDAC) is one of the most aggressive human malignancies, ranking 4th among causes of cancer-related death in the Western world [1].

Unlike most of the more frequent causes of cancer mortality (lung, colon, prostate and breast cancers) whose death rates are declining, the death rate for pancreatic cancer is relatively stable. The poor prognosis is reflected by a median survival of 5-8 months and a 5-year survival of less than 5% when all stages are combined [1-3].

PDAC and its variants account for over 90% of pancreatic malignancies and is characterized by a rapid disease progression and absence of specific symptoms, largely precluding an early diagnosis and curative treatment [3, 4]. In most cases, PDAC is already locally advanced at time of diagnosis and only approximately 10%-20% of patients are considered candidates for curative resection [1, 5]. The majority of patients (50%-60%) present with metastatic disease, and thus palliative chemotherapy remains the only option for almost all of these patients [6]. Owing to the high recurrence rate, surgical PDAC patients require adjuvant chemotherapy with or without radiotherapy providing a 5-year survival rate of 15%-25% [7]. Due to the described overall prognosis for all pancreatic cancer patients, systemic chemotherapy, radiation therapy or a combination of both is used following surgical resection (adjuvant therapy) and also prior to the tumor resection (neoadjuvant therapy) to improve cure rates.

So far, gemcitabine monotherapy was the only accepted treatment worldwide. Based on current data, it is clear that treatment with gemcitabine or 5-fluorouracil results in a median survival of just a few months [8, 9]. The

limitation of this treatment is mainly due to the profound resistance of PDAC cells towards anti-cancer drugs, emerging from the efficient protection against chemotherapeutic drugs by an altered balance of pro-and anti-apoptotic proteins, which results in a markedly reduced apoptotic responsiveness [10, 11].

The limited therapeutical options were recently enriched, after the results of a large study that demonstrated survival benefit of patients with advanced pancreatic cancer treated with combination of oxaliplatin, irinotecan and 5-fluorouracil (FOLFIRINOX), though this regimen was well tolerated only by very fit patients, which is not often the case in this disease [12]. Since the efficacy of most cytotoxis is at least very modest, if not disappointing, the efforts lie on the addition of biological or novel agents to gemcitabine, hoping to find a pivotal pathway which may play role in this disease [13]. Currently there are around 1070 clinical trials focusing on studying new biomarkers, different drug combinations and vaccines designed for pancreatic cancer (www.clinicaltrial.gov).

There is a great need for relevant preclinical models to test potential therapeutics in the treatment of pancreatic cancer. The use of animal models that mimic biological processes of cancer seen in human disease is paramount in testing potential therapeutics.

The subcutaneous (s.c.) implantation of human pancreatic cancer cell lines in SCID or nude mice (xenograft) has been commonly used in many studies for preclinical efficacy testing of novel therapeutic agents *in vivo*, and results are typically extrapolated for human cancer. However, because of the great dissimilarity of the host environments, many original biological characteristics of the human cancer cells become lost and many therapy-related environmental factors cannot exert their effects in such models (e.g.,

the human pancreatic tumor cells seldom metastasize when implanted in the subcutaneous site [14, 15]). This may explain, in part, why many novel antitumor agents active in the subcutaneous animal model are ineffective in treating human cancer. Thus, it can be argued that cancer treatment should be evaluated using tumors growing in their organ of origin (orthotopic transplantation), where tumor structure, vasculature, physiology, and growth pattern more closely mimic the clinical disease processes. In subcutaneous models, caliper measurement or tumor weights made at final autopsy are the generally used assessment methods [16]. In orthotopic models these assessments can only provide the terminal results without any information regarding tumor development. To fully utilize the potential of clinically relevant orthotopic models in experimental drug development, a noninvasive observation method is needed to detect tumor development in the mouse pancreas and serially monitor tumor growth kinetics.

In the last years noninvasive methods have become available to monitor tumor growth serially at internal sites in small rodents. Advancements in small animal imaging strategies have arisen both from modifications to structural and functional imaging modalities that are used clinically and the development of several novel modalities that are well suited for the study of animal models of human disease. The more traditional modalities that have been applied to laboratory animal models include ultrasounds (US), magnetic resonance imaging (MRI), positron emission tomography (PET), single photon emission computed tomography (SPECT), computed tomography (CT), and optical modalities (bioluminescence imaging (BLI) and FLI).

In vivo BLI is one of the newer methods for *in vivo* assessment that is well suited for animal models, is accessible to investigators and offers versatility for the *in vivo* detection of bioluminescent reporter genes. This method allows

sensitive and quantitative detection of cells noninvasively in laboratory animals: it enables to noninvasively follow molecular and cellular events that lead to tumorigenesis and disease progression and rapidly reveal therapeutic efficacy in preclinical studies of novel therapeutic strategies. As such, this technology can be used to refine animal models and aids in the discovery and development of new and improved clinical cancer prevention and treatment regimens.

Bioluminescence refers to the enzymatic generation of visible light by living organisms. The most commonly used bioluminescent reporter gene for research purposes has been luciferase from the North American firefly (*Photinus pyralis*; Luc). This reporter has been modified for optimal expression in mammalian cells and used for many years in bioassays for adenosine triphosphate (ATP) quantification, and to study gene expression in transfected cells in culture [17]. Luciferase catalyses the transformation of its substrate d-luciferin into oxyluciferin in an ATP-dependent process, leading to the emission of photons, which can be detected using low-light sensing instruments, including standard luminometers. Extending the use of luciferase as an optical reporter, from biochemical and cell culture assays to living animals, was dependent upon development of low light imaging systems based on charge coupled device (CCD) cameras and two other key observations. The first observation was the demonstration that the *P. pyralis* luciferase diffuses within minutes throughout all tissues after intravenous (i.v.) or intraperitoneal (i.p.) administration and rapidly enters many cell types [18]. The second finding was that the level of photon emission and the spectrum of emitted light from Luc+-expressing mammalian cells is adequate to penetrate tissues of small research animals, such as mice and rats, and can be detected externally with low-light imaging cameras [19]. Recent

improvements in the detection technology have led to the development of in vivo imaging systems that employ ultra-sensitive cooled CCD cameras [20].

BLI of neoplastic tissue requires the gene, encoding the bioluminescent reporter protein, to be transferred to cells of interest, which can be accomplished using any number of standard gene transfer methods [21, 22, 23]. Cells with stable expression of luciferase are injected into the research animal and the light emitted from the tagged cells can be monitored externally. To generate such an image, the animals are anaesthetized and placed in a light tight chamber equipped with the CCD camera. A grayscale reference image (digital photograph) is acquired under weak illumination, then in complete darkness the photons emitted from the body of the animal are detected externally using a range of integration times from 1 second to 5 minutes. The data are transferred to a computer equipped with image acquisition and analysis software for quantification [19]. To display the anatomical origin of photon emission, a pseudocolor image representing light intensity (from blue for least intense to red for most intense) is generated and superimposed over the grayscale reference image. In this way cells can be localized even deep within tissues and the amount of photons detected externally can be used to estimate the number of Luc+ cells within the animal.

With advancements in detectors, it is now possible by using BLI to quantitatively and non-invasively examine *in vivo* tumor growth and regression, with great sensitivity and a broad dynamic range.

Moving to another imaging methodology, Magnetic Resonance Imaging (MRI) is a non-invasive imaging technique, which is widely used in the field of medical imaging with great potentials for the diagnosis and therapy of human tumors, both in the clinical and experimental setting. Very similar

methods of assessment can be applied to humans and animal models, making MRI a unique tool in preclinical studies. The great advantage of this technique resides in its non-invasiveness, insuperable soft tissue contrast and multiplanar capability. MRI is based on the physical principles of nuclear magnetic resonance (NMR) and tissue appearance depends on a combination of physical (e.g. proton density) and chemical (e.g. types of molecular interactions) properties of the water molecules. Two-dimensional images can be obtained in different planes and orientations of the sample under investigation and volume images (three-dimensional data sets) allow measurement of volumes.

A brief overview of NMR and MRI theory can be found in Appendix 1 of this thesis.

The evaluation of tumor response to oncologic treatments has traditionally been made according to response criteria based on morphologic imaging assessments such as those proposed by the Response Evaluation Criteria in Solid Tumors (RECIST) and Response Assessment in Neuro-Oncology Working Group [24, 25]. However, there is growing evidence that size assessments have significant limitations in situations where tumors cannot be measured, where there is poor measurement reproducibility, and where mass lesions persist following therapy [26]. As a result, more sophisticated measurement criteria and new imaging approaches are being applied to evaluate therapy response, including changes in tumor perfusion and cellular density [27]. With the increasing clinical use of cytostatic and novel biologic targeted agents, it has become increasingly recognized that new methods of therapy assessment that can inform about the likelihood of therapeutic success need to be urgently developed.

One of such methods is diffusion-weighted imaging (DWI), which explores the random motion of water molecules in the body. Water molecules held in a container outside the body are in constant random brownian motion and this uninhibited motion of water molecules is free diffusion. By contrast, the movement of water molecules in biologic tissues is restricted because their motion is modified and limited by interactions with cell membranes and macromolecules. In biologic tissues, the DWI signal is determined from the motion of water molecules in the extracellular space, the intracellular space, and the intravascular space [28] (fig. 1). Not surprisingly, given a unit time, water molecules in the intravascular space will have a greater diffusion distance because of blood flow than those in the extracellular and intracellular spaces. Clearly, the contribution of intravascular water diffusion to the measured DWI signal can vary among tissues. In tumors showing increased vascularity, the contribution of intravascular water diffusion to the MR signal may account for a significant proportion [29]. The degree of restriction to water diffusion in biologic tissues is inversely correlated to the tissue cellularity and the integrity of cell membranes [30–33]. Since tissue water movements are not ‘‘free’’ but restricted by cellular structures and other molecules, the measure of tissue water diffusivity is often termed the apparent diffusion coefficient (ADC). The ADC is derived from an exponential decay of the MR signal versus b-factor, which determines sensitivity of the sequence to water movements, with the implicit assumption that the probability density function of the diffusion process is Gaussian (i.e., free diffusion). When restrictions or hindrance of water molecules are present, such as in biological material, this interpretation cannot lead to a correct description. Therefore, the word ‘‘apparent’’ was included in the acronym ‘‘ADC’’ to highlight that the ‘‘real’’ diffusion coefficient of water is not obtained.

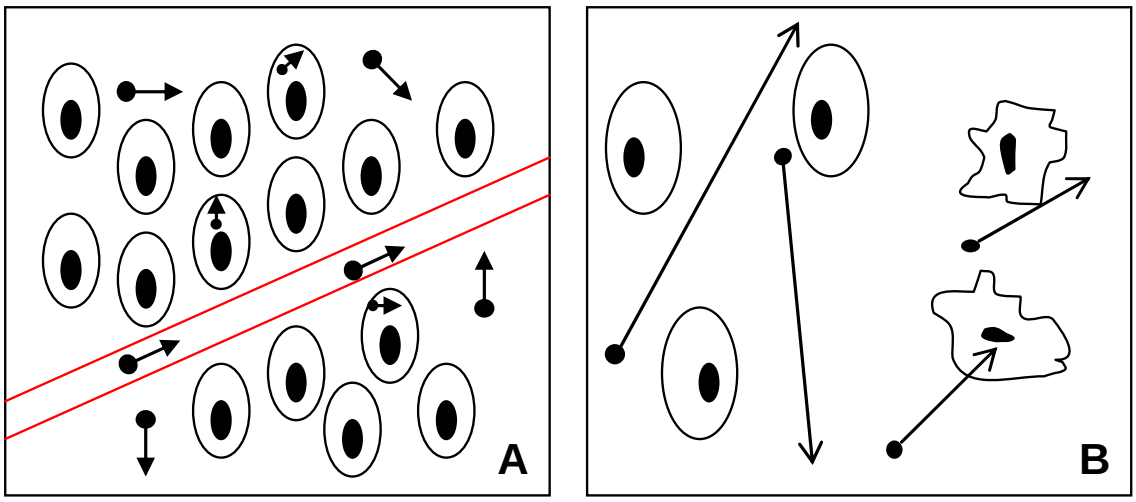

Figure 1. A) Restricted diffusion: cellularity and intact cell membranes. Drawing represents one voxel of tissue evaluated by diffusion weighted imaging (DWI) containing cells and blood vessel. Note water molecules (black circles with arrows) within extracellular space, intracellular space, and intravascular space, all of which contribute to measured MR signal. In this highly cellular environment, water diffusion is restricted because reduced extracellular space and by cell membranes, which act as barrier to water movement. B) Free diffusion: low cellularity and defective cell membranes. In less cellular environment, relative increase in extracellular space allows freer water diffusion than more cellular environment would. Defective cell membranes also allow movement of water molecules between extracellular and intracellular spaces.

The motion of water molecules is more restricted in tissues with a high cellular density associated with numerous intact cell membranes (e.g., tumor tissue). The lipophilic cell membranes act as barriers to motion of water molecules in both the extracellular and intracellular spaces. By contrast, in areas of low cellularity or where the cellular membrane has been broken, the motion of water molecules is less restricted. DWI yields qualitative and quantitative informations that provide unique insight into tumor characteristics, and there is growing evidence for its use in the assessment of cancer in the clinic, for both detection and staging.

Stejskal and Tanner [34] described an MR experiment that could be applied to the detection and quantification of water diffusion *in vivo*. They adapted a standard T2-weighted spin-echo sequence by applying asymmetric pair of

diffusion-sensitizing (bipolar) gradients around the 180° refocusing pulse (Fig. 2). That approach is now the basis of many DWI sequences in clinical use today. Static molecules acquire phase information from the first diffusion gradient, but information will be rephased by the second diffusion gradient without a significant change in the measured signal intensity. By comparison, moving water molecules acquire different phase information from the first gradient, but because of their motion, their signal will not be completely rephased by the second gradient, thus leading to a signal loss. Hence, the motion of water molecules is detected as attenuation of the measured signal intensity at DWI. The degree of water motion has been found to be proportional to the degree of signal attenuation. The sensitivity of the DWI sequence to water motion can be varied by changing the gradient amplitude, the duration of the applied gradient, and the time interval between the paired gradients. On clinical MR scanners, the diffusion sensitivity is easily varied by changing the parameter known as the "b value," which is proportional to these three factors. When the b value is changed, it is usually the gradient amplitude, rather than the duration or time intervals between gradients, that is altered. Water molecules with a large degree of motion or a great diffusion distance (e.g., within the intravascular space) will show signal attenuation with small b values (e.g., b = 50–100 s/mm^2). By contrast, large b values (e.g., b = 1,000 s/mm^2) are usually required to perceive slow-moving water molecules or small diffusion distances because these show more gradual signal attenuation with increasing b values. Hence, the information provided by DWI reflects changes that are occurring at a cellular spatial scale. For this reason, DWI is perceived as an advantageous tool for evaluating changes in the tumor microenvironment, both before and after treatment.

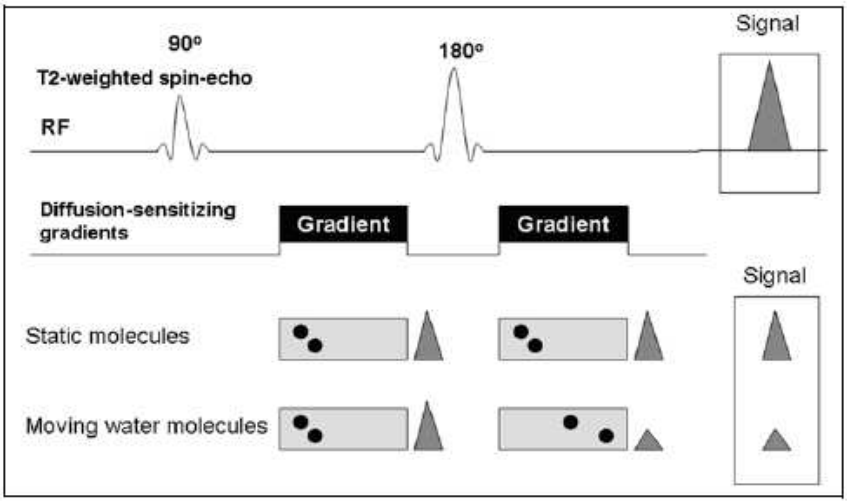

Figure 2. Measuring water diffusion: Stejskal and Tanner adopted T2-weighted spin-echo sequence for measuring water diffusion. They applied symmetric diffusion-sensitizing gradient around 180° refocusing pulse. On this schematic drawing, stationary molecules are unaffected by gradients and measured signal intensity is preserved. By contrast, moving water molecules acquire phase information from first gradient, which is not entirely rephrased by second gradient, thereby leading to signal loss. Hence, water diffusion is detected as attenuation of measured MR signal intensity. RF= radiofrequency pulse.

Tumors are frequently more cellular than the tissue from which they originate and thus appear to be of relatively high signal intensity (restricted diffusion) at DWI. One of the main applications of DWI outside brain is for the detection of liver metastases [35]. Metastases appear as high-signal-intensity foci at DWI. Nasu et al. [36] found that DWI was more accurate than superparamagnetic iron oxide (SPIO) enhanced MRI for the detection of liver metastases. In another study, DWI was found to have high sensitivity and specificity for the detection of colorectal hepatic metastases [37].

Tumors differ in their cellularity, and this difference may reflect their histologic composition and biologic aggressiveness. The use of DWI for tumor characterization is therefore largely used in the evaluation brain tumors [38].

In the liver qualitative visual assessment can help to distinguish cystic from solid lesions. However, it is often difficult to distinguish different types of solid lesions from one another in the liver by visual assessment alone. For example, a hemangioma will exhibit restricted diffusion and can mimic the appearance of a metastasis at DWI. Using quantitative evaluation, investigators have found that benign liver lesions, such as cysts and hemangiomas, have higher mean ADC values than malignant lesions, such as metastases and hepatocellular carcinoma [39, 40].

The ADC has also been used to distinguish abscesses, which have low ADC values, from cystic and necrotic metastases, which have higher ADC values [41].

In the abdomen, DWI has also been applied to characterize focal renal lesions [42, 43]. Because of the organization of the renal tubules, water diffusion in the normal kidney is anisotropic [44, 45]. DWI in the kidney can readily distinguish between cystic from solid renal lesions [42]. However, it is not yet possible to confidently distinguish malignant from benign renal neoplasms on the basis of qualitative assessment or ADC measurements [42].

Elsewhere, the ADCs of malignant breast lesions have been found to be lower than the ADCs associated with benign diseases [30, 46, 47], and DWI was able to distinguish cystic soft-tissue sarcomas from solid types [48]. More recently, DWI has also been found to be useful in detecting colorectal carcinoma [49] and showing cystic lesions of the pancreas [50] and ovaries [51].

There is increasing interest in the application of DWI for detecting tumor response. Effective anticancer treatment results in tumor lysis, loss of cell

membrane integrity, increased extracellular space, and, therefore, an increase in water diffusion (fig. 3) [52, 53].

The results of animal studies have confirmed that after the initiation of chemotherapy, radiation therapy, or novel therapy, an increase in the ADC value may be observed in those responding to treatment [54]. Furthermore, treatment effects can be observed within the first 24 hours after initiating treatment [29, 54] due to cell swelling, which results in a transient decrease in the ADC [29, 54]. Using ADC measurements, researchers who have studied hepatocellular carcinoma [55], cerebral gliomas [56], and soft-tissue sarcoma [57] have found that individuals who respond to treatment show a significant rise in the ADC values after therapy. In a recent study of hepatic metastases from colorectal carcinoma, an increase in ADC was observed in patients with at least a partial response to treatment [58]; however, an ADC increase was not observed in the nonresponders [58].

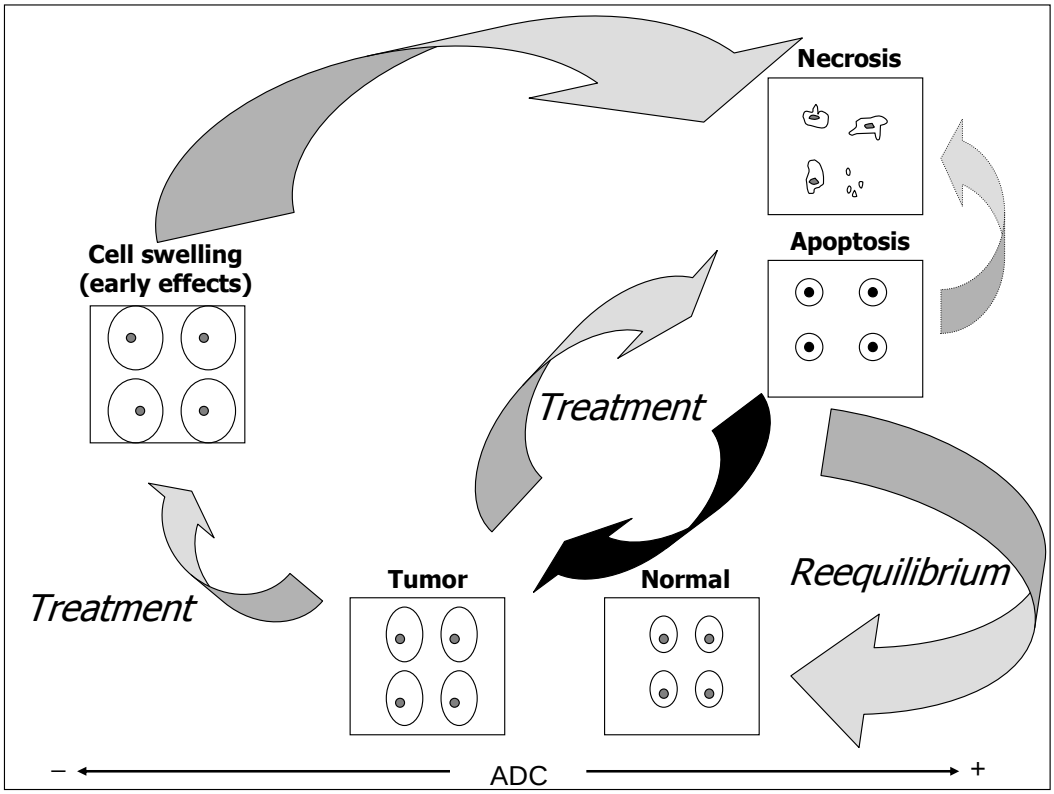

Figure 3. Schematic diagram shows variation in tumor apparent diffusion coefficient (ADC) with treatment. Soon after initiation of chemotherapy or radiation therapy, cell swelling occurs, which can lead to decrease in tumor ADC. This is followed by cell necrosis and lysis, resulting in cell shrinkage and increased ADC. This apoptotic tumor cells may also undergo secondary lysis (dotted arrow). After completion of treatment, there is process of reequilibrium with resorption of extracellular fluid, leading to decrease in ADC. Tumor regrowth (black curved arrow) can also result in decreased ADC.

DWI of the pancreas has been used in the evaluation of cystic and solid pancreatic tumors as well as neuroendocrine tumors of the pancreas (islet cell tumor) [59, 60, 61]. Studies of pancreatic adenocarcinomas reported that ADC values tend to be lower compared with normal pancreas [62, 63]. However, histopathology of the tumor may influence the ADC values and lesions with interstitial edema and loose collagen fibers actually had ADC values higher than the normal pancreas, while dense fibrosis and increased cellularity resulted in lower ADC values [64].

ADC values of mass-forming focal pancreatitis can be either lower or higher compared with pancreatic adenocarcinoma and indistinguishable from the remaining gland [62, 63]. This variability in ADC values and the overlap between gland and mass forming pancreatitis has been attributed to the nature of inflammation in mass-forming pancreatitis.

Pancreatic cysts on the other hand appear to be more distinguishable from the surrounding pancreas, compared with pancreatic adenocarcinoma. Studies of cystic lesions found that simple cysts and uncomplicated pseudocysts are isointense with background pancreas on images with a high b-value, whereas abscesses, hydatid cysts, and neoplastic cysts, such as mucinous cystadenomas and cystadenocarcinomas, reveal higher signal intensity [65].
From the preclinical point of view there are few reports on the use of MRI in orthotopic murine models of pancreatic cancer. In three of them [66, 67, 68] classical anatomical MRI together with administration of contrast agents was applied on different pancreatic models.

Although technically challenging, DWI in rats and mice in other body locations [69] has been attempted and reported by a number of study groups using clinical MRI scanners.

To the best of our knowledge only one publication [70] describes the use of DWI in attempt of correlating early ADC changes after treatment with mice survival in an orthotopic pancreatic model.

AIM OF THE THESIS

2 AIM OF THE THESIS

Adenocarcinoma of the pancreas is one of the most aggressive human malignancies. Better models to study tumor behavior *in vivo* are needed for the development of more effective therapeutics. In the attempt to create clinically relevant models for studying novel treatments directed against pancreatic cancer, we defined a methodology to measure the effect of antineoplastic compounds in established human pancreatic cancer orthotopic xenografts using different luciferized pancreatic cancer cell lines (MiaPaCa-2 and Capan-1) to allow both magnetic resonance and bioluminescence imaging of animals *in vivo*. Furthermore advanced MRI techniques, such as DWI, were applied to evaluate early response to therapy.

MATERIALS AND METHODS

3 MATERIALS AND METHODS

3. 1 In vitro studies

3.1.1 Cell lines and culture

Capan-1 cell line was first isolated by Fögh *et al.* at the Sloan Kettering Institute from a 40 years old Caucasian male in 1977. Cells were obtained from DSMZ (Deutsche Sammlung von Mikroorganismen und Zellkulturen) and cultured in RPMI 1640 medium supplemented with 10% fetal calf serum and 2 mM L-glutamine.

MIA-Pa-Ca-2 cell line was established by Yunis *et al*. from a 65 year old Caucasian male in 1975. The cell line was obtained from ECCC (European Collection of Cell Cultures) and cultured in DMEM medium supplemented with 10% fetal calf serum and 2 mM L-glutamine.

Both cell lines were incubated in a humidified 5% CO_2 incubator at 37°C. The medium was replaced with fresh medium as needed, and cells were maintained by serial passaging after trypsinization.

3.1.2 Luciferized cell lines and culture

Capan-1 cells were infected with the pLenti6.3-Luc2 lentiviral vector following the manufacture's protocol (ViraPower system, Invitrogen). In this vector, the luciferase gene Luc2 (Promega) was cloned in the pLenti6.3/V5-DEST lentiviral vector (Invitrogen) downstream of the CMV promoter. The pLenti6.3/V5-DEST vector harbors the blasticidin resistance gene; hence the cells that have integrated the pLenti6.3-Luc2 into their genome can be selected by growing cells in culture media containing the antibiotic blasticidin.

Mia-Pa-Ca-2 cells were co-transfected with two plasmids: the pGL4.13 and the p-CI-Neo plasmids (both from Promega) using Lipofectamine Reagent (Invitrogen). The pGL4.13 plasmid consists in the SV40 promoter driving expression of a luciferase gene (Luc2). This plasmid does not contain any antibiotic resistance gene and, therefore, cannot be used for the generation of a stable luciferase expressing cell line. To overcome this issue, the pCI-Neo plasmid, which harbors a Neomycin resistant gene, was also used. Because in co-transfection experiments normally both plasmids enter the transfected cell, cells that have integrated the pCI-Neo plasmid into their genome survive in cell culture media containing the antibiotic G418 and are expected to have integrated the pGL4.13 construct as well.

Single colonies were screened based on luminescence signal obtained with the IVIS-100 system. The resulting Capan-1-Luc2 cell line generated emitted 2300 photons/min/cell. The Mia-Pa-Ca-2-Luc cell line emitted 300 photons/min/cell.

3. 2 In vivo studies

3.2.1 Orthotopic murine model

Animal procedures were approved in a protocol by Nerviano Medical Sciences Care and Use Committee. Six-week-old male Balb Nu/Nu mice, weighting 25–33 g were obtained from Harlan Laboratories. The mice were acclimatized and housed in a sterile environment where cages, bedding, food and water were autoclaved and used to develop an orthotopic model bearing Capan-1 and Mia-Pa-Ca-2 cell lines, both normal and luciferized.

General anesthesia was performed using ketamine (70 mg/kg i.p.) + xylazine (6 mg/kg i.p.). A left lateral laparotomy was performed, and the spleen and

distal pancreas were mobilized. $2x10^6$cells suspended in approximately 50 µl phosphate-buffered saline (PBS) were injected into the pancreas. The abdominal incision was closed using a surgical staple, and analgesia was administered for immediate pain relief. After implantation, the mice were inspected daily for 1 week for any bleeding or wound complications.

3.2.2 Bioluminescence Imaging (BLI)

Luminescence was acquired weekly using the IVIS-100 (Xenogen) system. It consists of a charge coupled device (CCD) camera, an imaging chamber and a preconfigured computer. The camera is a scientific grade, back-thinned, back-illuminated, and thermoelectrically cooled. The imaging and the signal quantification were controlled by analysis and acquisition software Living Image (Xenogen).

For the imaging *in vivo*, mice were injected intraperitoneally with 150 mg/kg of D-luciferin in PBS and subsequently anesthetized (1-2% isofluoran). Anesthetized mice were placed after 12 minutes from luciferin injection on the heated platform (37°C) inside the imaging chamber with a continuously anesthetic delivery. Acquisition time varies between 10 and 60 seconds, depending on the cell line and on the growth level of the tumor. The lower levels of emission of tumor bioluminescent cells were detected, integrated, digitalized, and shown by the instrument. The region of interest (ROI) around the tumor was manually drawn and quantified in photons/second.

3. 2. 3 Magnetic Resonance Imaging (MRI)

MRI was acquired weekly on a 7 T Bruker Pharmascan.

For MRI, the mice were anesthetized with 2% isofluorane and positioned supine on a plexiglass animal bed. An orthogonally bent plastic board was tightly taped under the thoracic region to prevent the transfer of respiratory motion in the chest to the abdominal area, as shown in figure 4. A pneumatic sensor, connected to a triggering system (Bruker BioTrig), was placed on the thoracic area to monitor animal's breathing and minimize movement artifacts by triggering acquisition to expiratory phase of respiration.

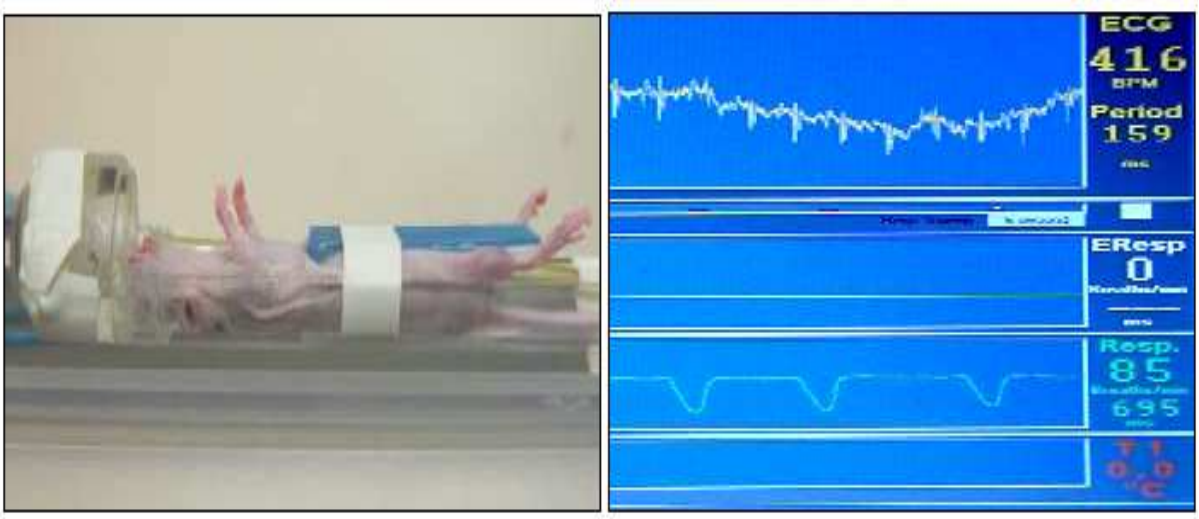

Figure 4. On the left a mouse ready for the MRI session: the blue plastic device was placed under the xiphoid cartilage to separate the abdominal area from the thoracic region. On the left the Biotrig system shows respiratory and cardiac parameters.

The animal bed was then inserted in the radiofrequency coil (38 mm internal diameter) and pilot spin echoes sequences on axial orientation were collected at the beginning of every MRI experiment.

Based on those scout images, multislice 2D T2-weighted fast spin echo sequences (Bruker Rapid Acquisition with Relaxation Enhancement: RARE)

were acquired in coronal (12 slices of 0.8 mm thickness; field of view 4x4 and spatial resolution of 156 µm) and axial orientations (14 slices of 0.8 mm thickness; FOV 4x4 and spatial resolution of 156 µm) for tumor visualization.

A gadolinium-based contrast agent was used. As a paramagnetic contrast agent, it alters the MR signals from vascularized tissues by changing T1 tissue's relaxation rates and is expected to produce a positive contrast in T1-weighted images. Multislice 2D T1-weighted spin echo sequences (Bruker RARE) were used to visualize tumor tissue before and after i.v. administration of a gadolinium-based contrast agent (Gadovist®, dose: 0.3 mmol/Kg).

In the initial set-up of the MRI protocol Dynamic Contrast-Enhanced (DCE)-MR imaging sequences were also used. In this case T1-weighted images were serially acquired before, during and after the injection of the contrast agent, in order to span the time evolution of the agent's distribution and its eventual wash-out. In this case Gadovist® was administered as a bolus, via a catheter injection into the tail vein of the mice (dose: 0.3 mmol/Kg).
Diffusion weighted images were obtained by a diffusion sensitized Echo Planar Imaging (EPI) sequence with two b-factors (500 and 1000 s/mm²) at three orthogonal gradient directions (x, y, z), diffusion separation time: 16 ms, diffusion gradient duration: 7 ms, FOV 4x4, 128x128 matrix, spatial resolution 312 µm.

The final acquisition protocol for the efficacy experiment was as follows:

- RARE T2-W: TR/TE = 3000/14 ms, 256×128 matrix, 8 averages, rare factor 8, 0.8 mm slice thickness

- EPI-diffusion trace: TR/TE = 3000/34 ms, 128x128 matrix, 1 average, Δ=16, δ=7, 1 mm slice thickness, 6 slices
- RARE T1-W (acquired before and 10 minutes after contrast agent injection): TR/TE = 600/12 ms, TE eff= 24 ms, 256×128 matrix, 12 averages, rare factor 4, 0.8 mm slice thickness

3.2.4 Efficacy study

For the efficacy study the MiaPaCa-2-luc tumor bearing mice were randomized and divided into two groups, according to BLI observations:

- Group 1 (5 mice) was the control group and was given glucose saline solution only;
- Group 2 (6 mice) received Irinotecan, dissolved in glucose saline solution at 5%, according to the following schedule: 60 mg/kg/i.v. q4dx6, which correspond to day 13, 17, 21, 25, 29, 33 from orthotopic injection.

Irinotecan (CPT11, Camptosar®) is a topoisomerase-I inhibitor that impedes the DNA helix tortional stress-relieving activity of DNA topoisomerases and also prevents their release from the DNA thus prompting apoptosis.

The imaging acquisition time points were:

- Bioluminescence: day 8, 13 (start T), 24, 31, 41 from orthotopic injection;
- Magnetic Resonance: day 15, 21, 28, 34, 42 from orthotopic injection.

3.3 Histology

Histological analysis was performed at different stages of tumor progression to investigate tumor phenotypes and validate MRI findings. Animals were sacrificed by CO_2 euthanasia and necropsy was performed. Gross findings were evaluated and recorded. The pancreatic tumors were excised and fixed in 10% buffered formalin. After 48 hours, tissues were transferred to 70% ethanol and embedded in paraffin. Formalin-fixed paraffin-embedded specimens were serially sectioned and slide-mounted. Sections were stained with hematoxylin and eosin (H&E) for histopathological studies.

3.4 Statistics

Data are expressed as mean ± standard deviation, unless stated otherwise. Differences between two groups of continuous data were assessed by the unpaired (independent-sample) Student's *t*-test. The mean tumor volumes were compared for all groups using one-way ANOVA. Statistical significance was defined as $p < 0.05$.

RESULTS

4 RESULTS

4. 1 Establishment of murine orthotopic models of pancreatic cancer

The transplantation surgical procedure used in this work efficiently provided the creation of orthotopic murine models of pancreatic cancer from Capan-1 and Mia-Pa-Ca-2 luciferized and non-luciferized cell lines, as all transplanted mice developed tumors. The efficiency of cellular engraftment was proved by BLI examination, which provided informations about cells viability, as soon as day 2 from pancreatic injection.

4. 2 Imaging characterization of orthotopic models of pancreatic cancer

The tail of mouse pancreas lies near two solid organs, stomach and spleen, which can be identified given their distinct shape and signal pattern in MRI. The spleen presents as a triangular dark object in coronal orientation, while the stomach is an oval structure with hollow cavities, continuing to the right into the duodenum and lying adjacent to the right lobe of the liver. Following the tail of the pancreas to the right allows delineation of the body of the pancreas, which lies immediately adjacent to the duodenum. In the healthy mouse the pancreas is not easily detectable; the implanted tumor cells were expected to grow in the space between stomach, spleen and duodenum, which can be used as landmarks, allowing visualization of the pancreatic parenchyma.

To visualize the orthotopic tumor a multislice T2-weighted spin echo sequence was used.

In figure 5 a coronal T2-weighted image of the abdominal cavity of a mouse is presented: it is possible to easily identify some of the abdominal organs, such as the liver (L) the stomach (S) and the cecum (C); between the liver and the stomach lies a little pancreatic tumor (dotted white line).

Contiguous slices of T2-weighted images, covering the suspected tumor site, in coronal (figure 6) and axial (figure 7) orientations are shown: the pancreatic tumors appeared hyperintense with respect to the surrounding anatomical structures. Tumors as small as 1.5 mm in diameter were detected.

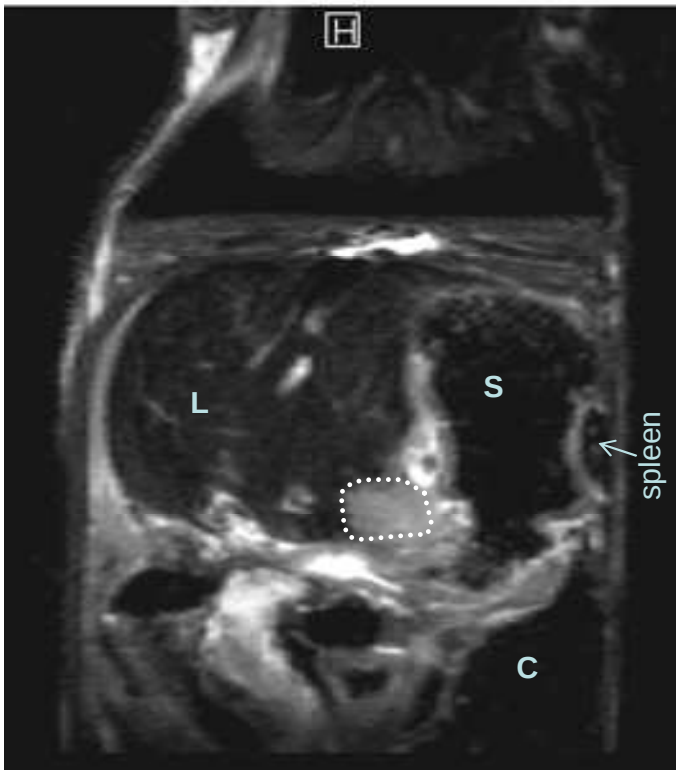

Figure 5. Coronal view of the abdominal cavity in a mouse: the dotted line indicates the pancreatic tumor, L= liver, S= stomach, C= colon

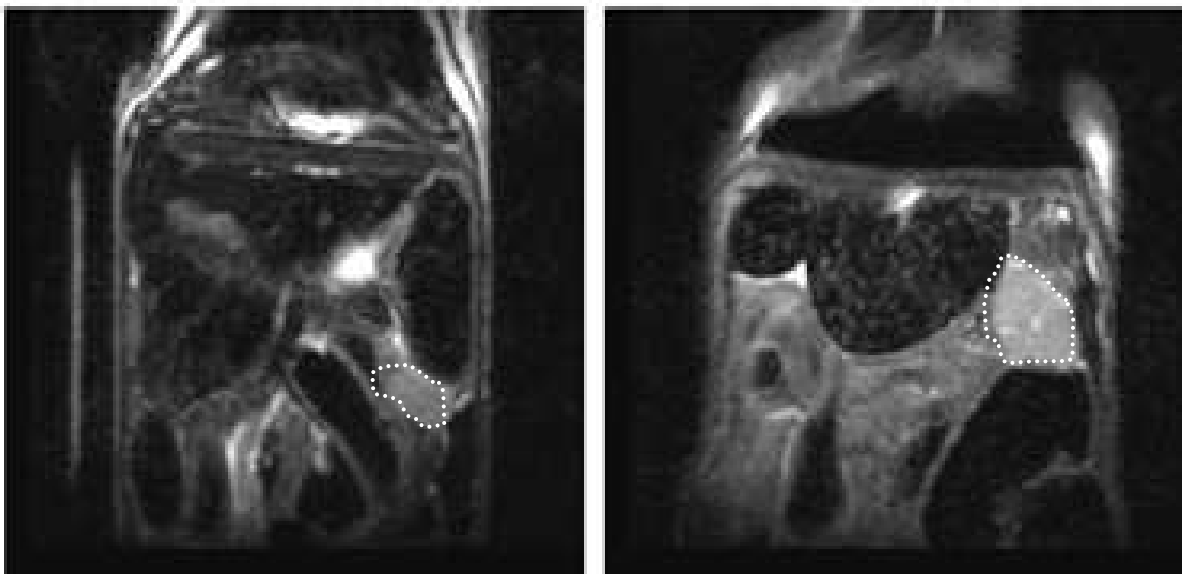

Figure 6. Representative T2-weighted images covering the pancreatic region in coronal orientation: the tumor is indicated by a white dotted circle.

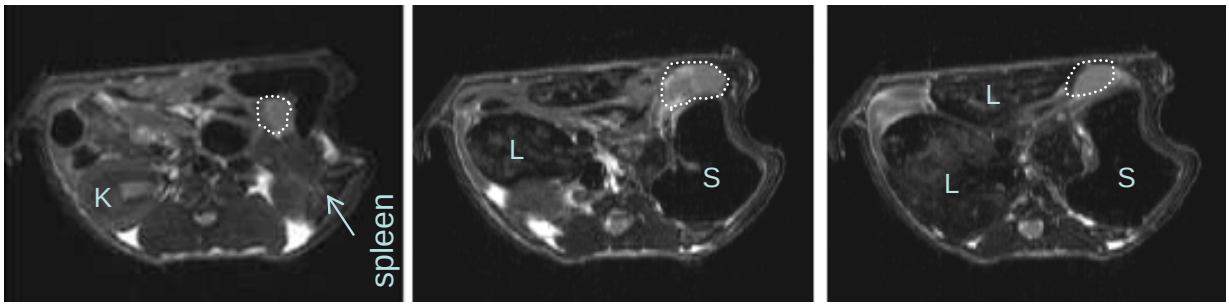

Figure 7. Representative T2-weighted images covering the pancreatic region in axial orientation: the tumor is indicated by a dotted circle, K= kidney, L= liver, S= stomach.

Besides capturing the morphological details of the tumor, serial acquisition of T2-weighted images allowed measurement of tumor volume for both cell lines used in this thesis. A macro was used to calculate tumor volumes (in cm^3) from single slice tumor areas and slice thickness. In fig. 8 a graph of tumor growth rates of the two luc-positive pancreatic adenocarcinoma cell lines is shown: MiaPaCa-2 tumors showed higher tumor growth rate than

Capan-1 tumors. MiaPaCa-2 parental (not luciferized) tumors showed faster growth with respect to the luciferized counterpart.

On the basis of the results of growth kinetics MiaPaCa-2-Luc tumors showed to be more suitable than Capan-1-Luc for efficacy studies.

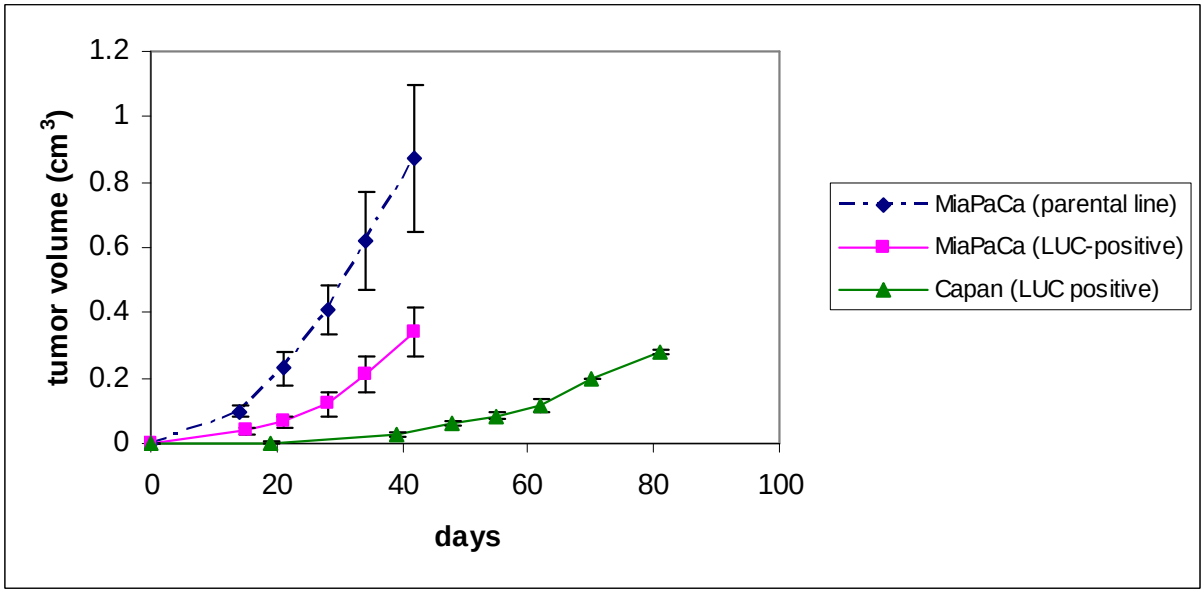

Figure 8. Tumor growth kinetics of implanted MiaPaCa-2-Luc (pink line) and Capan-1-Luc (green line) cell lines; parental Luc negative MiaPaCa-2 cell line (blue line) is also show for comparison.

To validate the accuracy of this measurement method, the last series of MRI tumor volume measurements were compared with tumor weight after necropsy (tumors were dissected immediately after imaging). These last MRI tumor volume measurements and tumor weights were strongly correlated (data not shown). This result suggests that MRI tumor volume measurements are accurate and reliable tools without invasive access to internal sites.

The use of the plastic device applied on the mouse body (fig. 4) together with the triggering system allowed the acquisition of high quality diffusion EPI

images. In fig. 9 a set of diffusion weighted images obtained at different b-values in a mouse bearing a Mia-Pa-Ca tumor is shown.

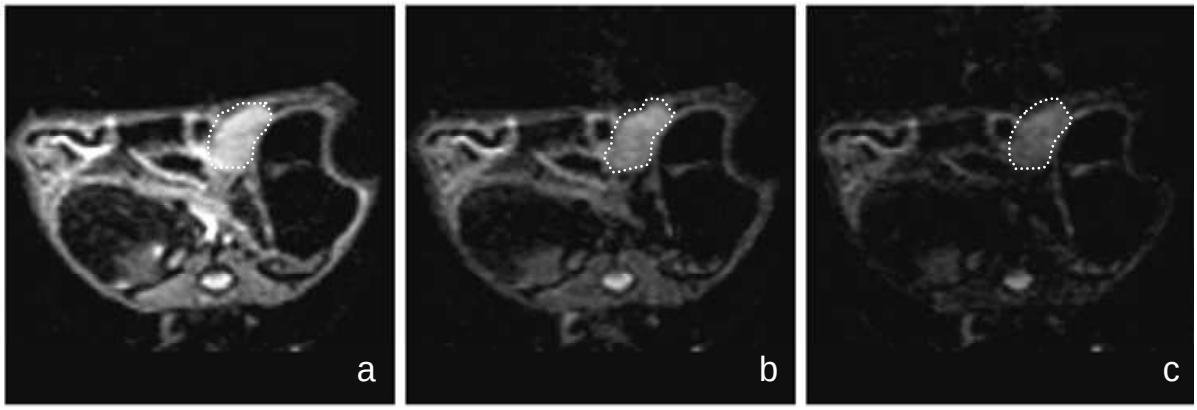

Figure 9. Representative diffusion-weighted images of a mouse bearing a Mia-Pa-Ca-2 tumor at two different diffusion-weighting factors: b = 500 s/mm2 (b), b = 1100 s/mm2 (c), and b=0 image (a) with constant gray scale.

As tumors reached big volumes it was possible to highlight areas with different diffusion coefficient inside them, which corresponded to necrotic areas, identified also on T2-weighted images. In figure 10 diffusion-weighted images of a late stage tumor are presented: the viable area (light blue dotted line) maintains its high signal intensity at both weighting factors (fig. –B and –C). On the other hand the necrotic region shows greater signal intensity suppression with increased diffusion weighting (increased b-values), demonstrated also in the graph, where regions of interest, drawn in the two different areas, are plotted. The slope of the signal decay fitted through corresponding values for the necrotic region (red line) shows higher grade with respect to the viable one (yellow one), as expected in areas with increased water motility caused by cellular membrane disruption.

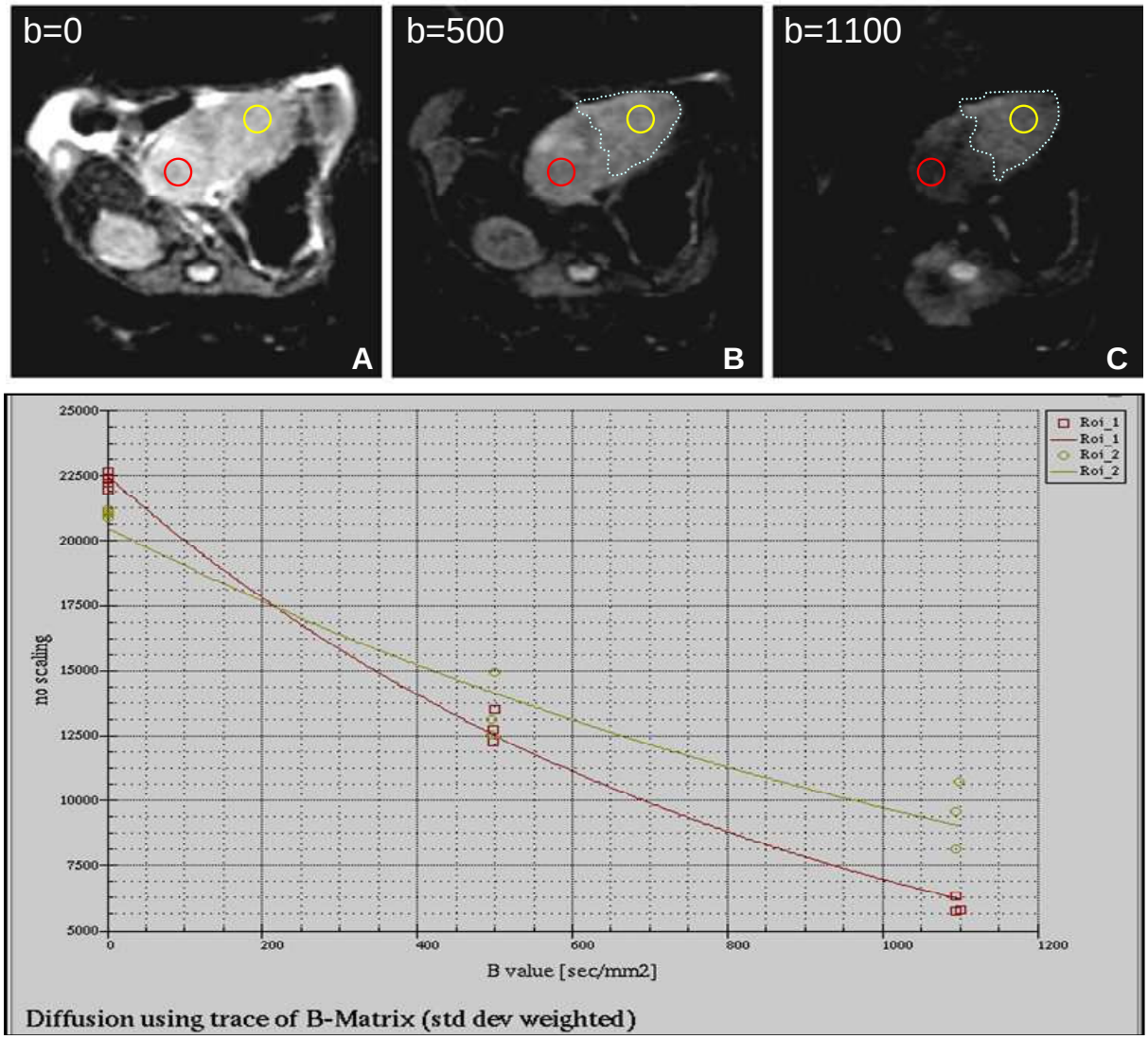

Figure 10. Diffusion weighted images of a big tumor. The light blue dotted line delineates the viable area of the tumor. Two regions of interest were drawn: one in the viable area (yellow) and the other one in the necrotic part (red). Graph shows signal attenuation of ROIs for the viable region (yellow line) and necrotic region (red line) of the tumor with increasing b-values.

In pre-contrast T1-weighted images, with the same acquisition geometry of T2-W, pancreatic tumors could not be distinguished from surrounding normal tissue, appearing isointense, as shown in figure 11.

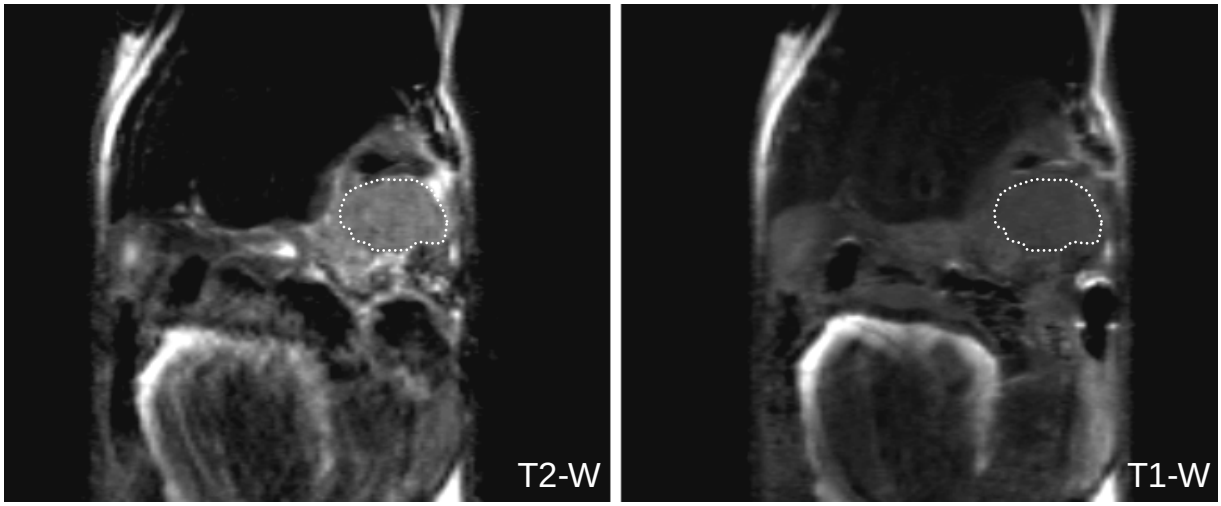

Figure 11. On the left a T2-weighted coronal image of a MiaPaCa tumor (dotted white circle) that shows a certain grade of hyperintensity with respect to the surrounding anatomical structures. On the right the same tumor in a T1-weighted image where no difference in signal intensity of the tumor is detectable.

The systemic injection of a contrast agent resulted in a very slight tumor enhancement, as depicted in fig. 12 (a= pre and b= post contrast T1-W images), while the highest Gd uptake was detectable in the visceral peritoneum.

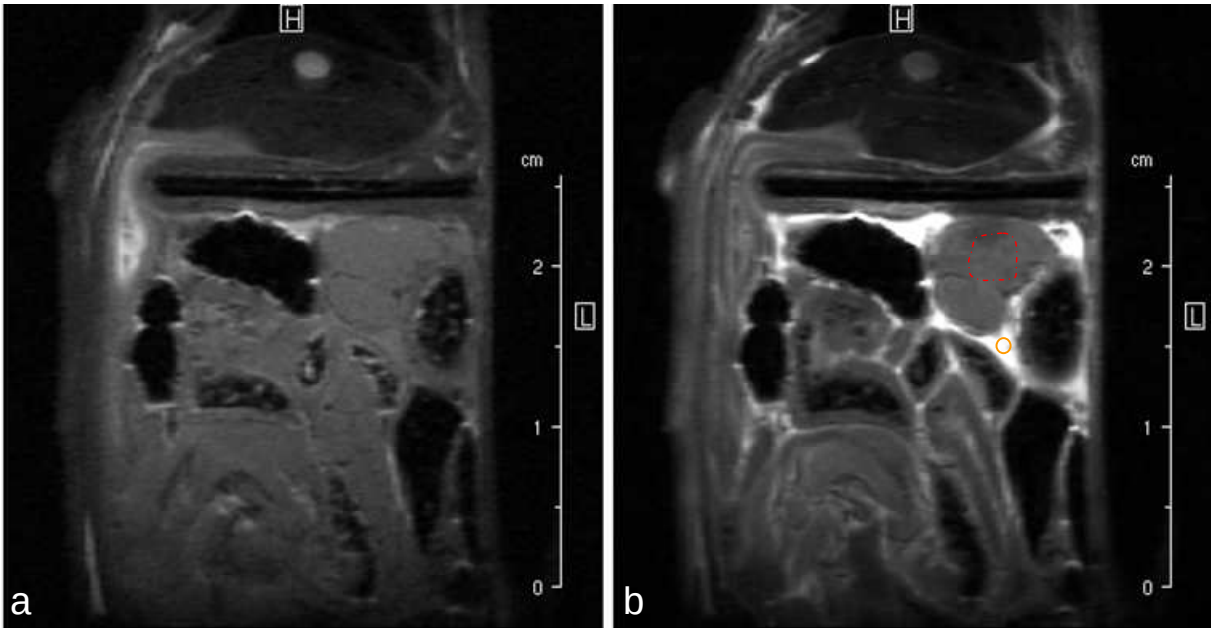

Figure 12. T1-weighted coronal images pre (a) e post i.v. injection of contrast agent.

In fig. 13 the enhancement time course of two regions of interest (ROI) obtained in DCE experiments is shown: ROI-1 (red circle) was drawn in the pancreatic tumor, ROI-2 (yellow circle) in the visceral peritoneal fat. This finding is in line with reported low enhancement rates observed in pancreatic tumors.

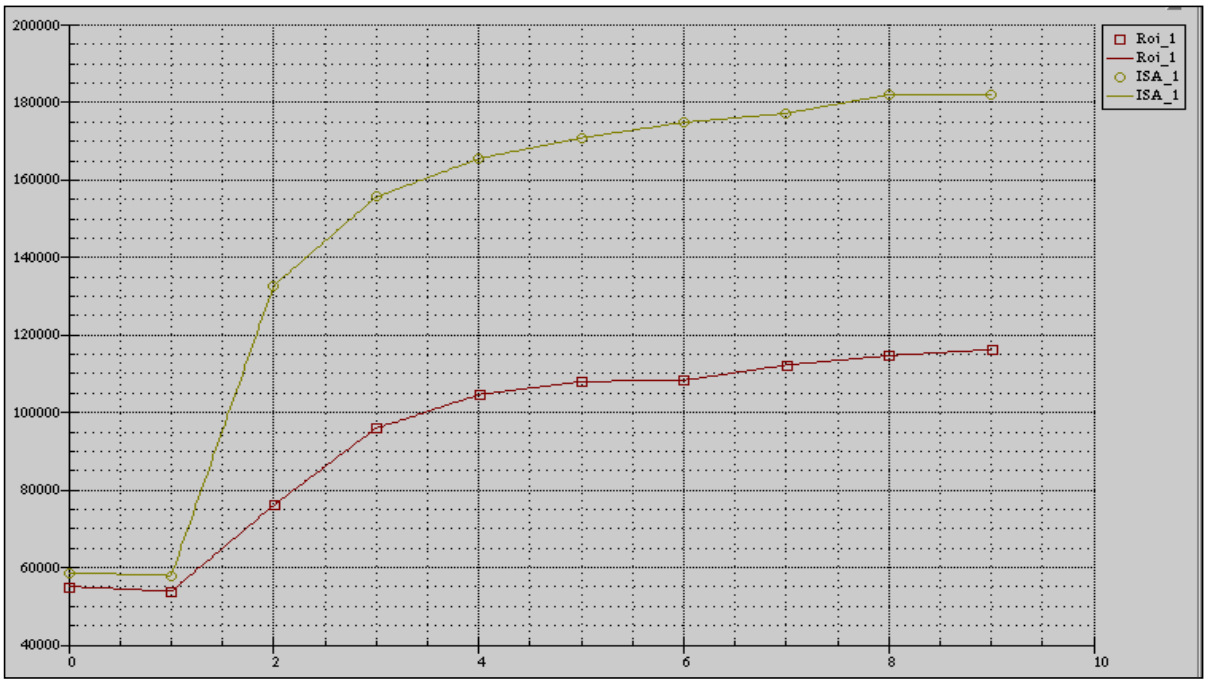

Figure 13. Time course of enhancement of ROIs drawn inside pancreatic tumor in red and visceral peritoneum in yellow.

4. 3 Histology

Histological examination of the H&E sections showed that Capan-1 cell line implantation in the pancreas resulted in multicentric locally extensive and infiltrative tumors. Up to 60% of the pancreatic tissue was effaced by a poorly demarcated, unencapsulated, multinodular mass, infiltrating and compressing adjacent parenchyma. The mass was composed by tubules embedded in a thick fibrous stroma (scirrous response). Tubules were lined by 1-2 rows of

cuboidal cells, with distinct cell borders, an intermediate N/C ratio and a moderate amount of pale eosinophilic homogeneous cytoplasm. Nuclei were basal, paracentral, round, with marginated chromatin and 1-2 evident nucleoli (neoplastic epithelial cells). Tubular lumina were filled by sloughed epithelial cells, erythrocytes, necrotic debris and/or by neoplastic cells arranged in infolded papillae. Anisocytosis and anisokaryosis were moderate. Mitoses were rare. Capan-1 cell line implantation in the pancreas resulted in multicentric locally extensive and infiltrative tumors, which were classified as moderately differentiated, tubulo/papillary pancreatic adenocarcinomas (fig. 14-A).

MiaPaCa-2 cell line implantation in the pancreas resulted in multicentric locally extensive and even more infiltrative tumors. Pancreatic parenchyma is almost completely effaced by a densely cellular mass, with only few spared normal acini and tubules embedded. The tumor is composed by solid areas of neoplastic cells, with scant fibrovascular stroma. Atypical cells are polygonal, with variably distinct cell borders, an intermediate N/C ratio and a moderate amount of eosinophilic homogeneous cytoplasm, lacking zymogen granules. Nuclei are paracentral, oval, occasionally indented, with marginated chromatin and one evident magenta nucleolus (neoplastic epithelial acinar cells). Anisocytosis and anisokaryosis are mild. Mitoses are 2-3 hpf, often with bizarre morphology. MiaPaCa-2 cell line implantation in the pancreas resulted in multicentric locally extensive and even more infiltrative tumors than Capan-1, which were classified as poorly differentiated, solid, pancreatic adenocarcinomas (fig. 14-B).

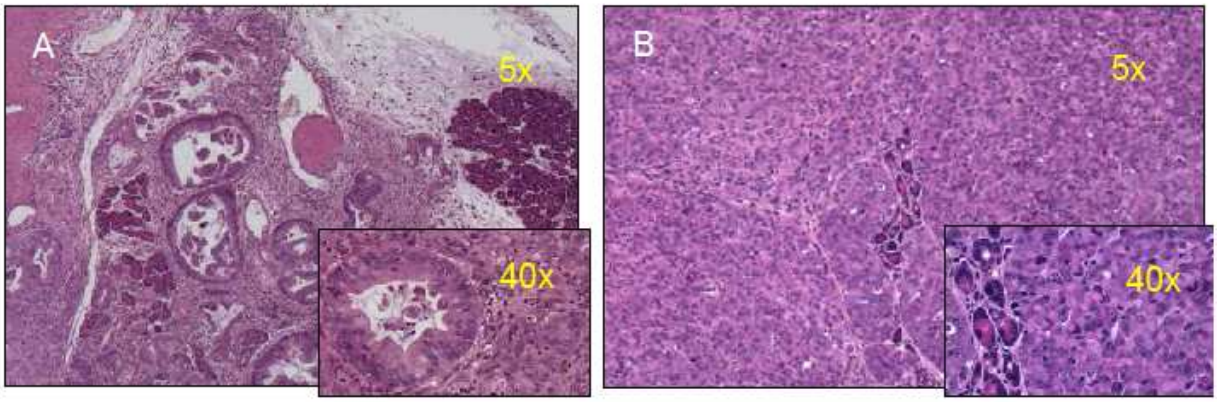

Figure 14. Examples of a Capan-1 tumor (A) and a MiaPaCa-2 tumor (B).

On the basis of the growth kinetic characteristics and of the histopathologic findings the MiaPaCa-2 model was selected for the efficacy study.

4. 4 Efficacy study

An example of temporally taken T2-weighted images of a control mouse (G1) and Irinotecan treated mouse (G2) is presented in figure 15, top: G1 and bottom: G2. The images refer to the central slice of the same tumor at different time points during the treatment course.

By using these images, we were able to build individual tumor growth curves for each tumor, which were employed to quantitatively assess tumor therapeutic response. A representative tumor growth curve for both groups is shown in fig. 16. The tumors of the control mice grew exponentially and resulted in large tumor volumes at the end of experiment, while all animals of Group 2 responded to the treatment with a strong tumor regression (85% tumor growth inhibition = TGI) at the end of treatment.

Similar percentages of tumor growth inhibition (86%) were obtained by BLI analysis, as shown in fig. 17, where BLI images of a representative control mouse (top) and of an Irinotecan treated mouse (bottom) during treatment are shown. To display the anatomical origin of photon emission, a pseudocolour image representing light intensity (from blue for least intense, to red for most intense) is generated and superimposed over the grayscale reference image. In this way cells can be localized even deep within tissues and the amount of photons detected can be used to estimate the number of Luc+ cells within the animal. In fig. 17-, averaged BLI measurements for G1 and G2 groups are plotted in graph. A good correlation was found between BLI and MRI evaluations in terms of TGI.

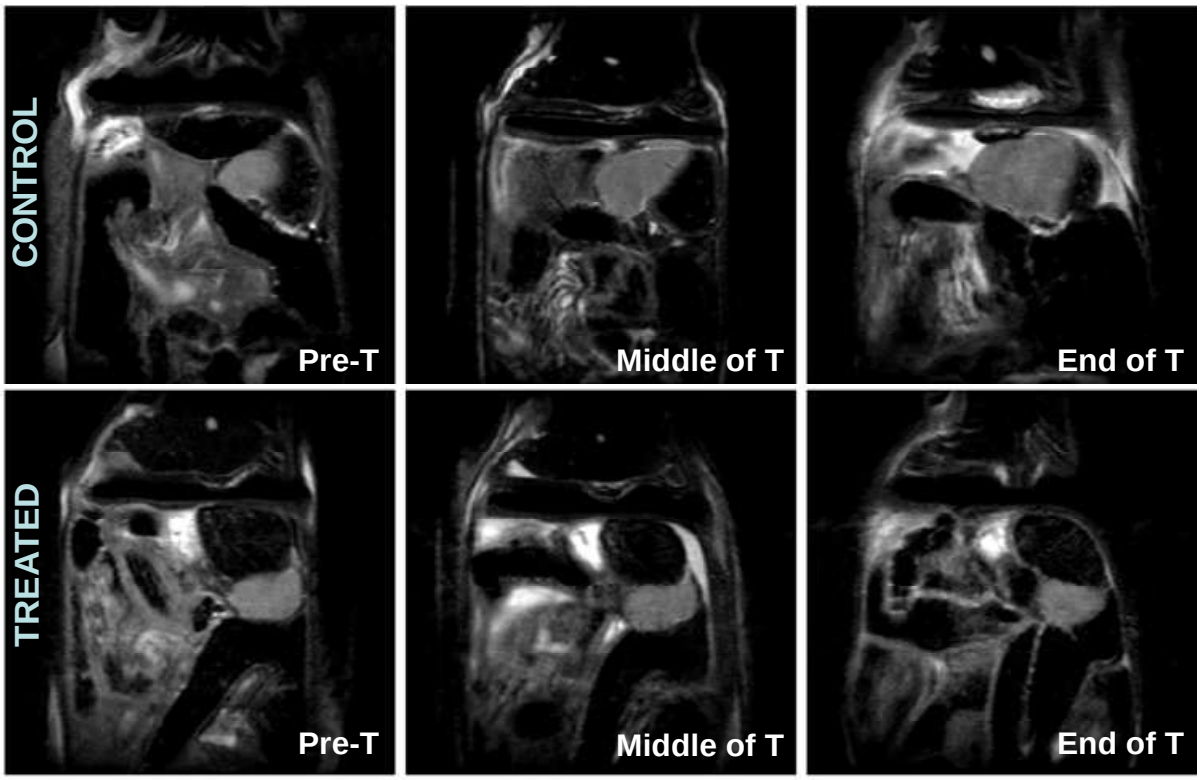

Figure 15. T2-weighted serial coronal images of a control mouse (top) and a treated mouse (bottom)
during treatment.

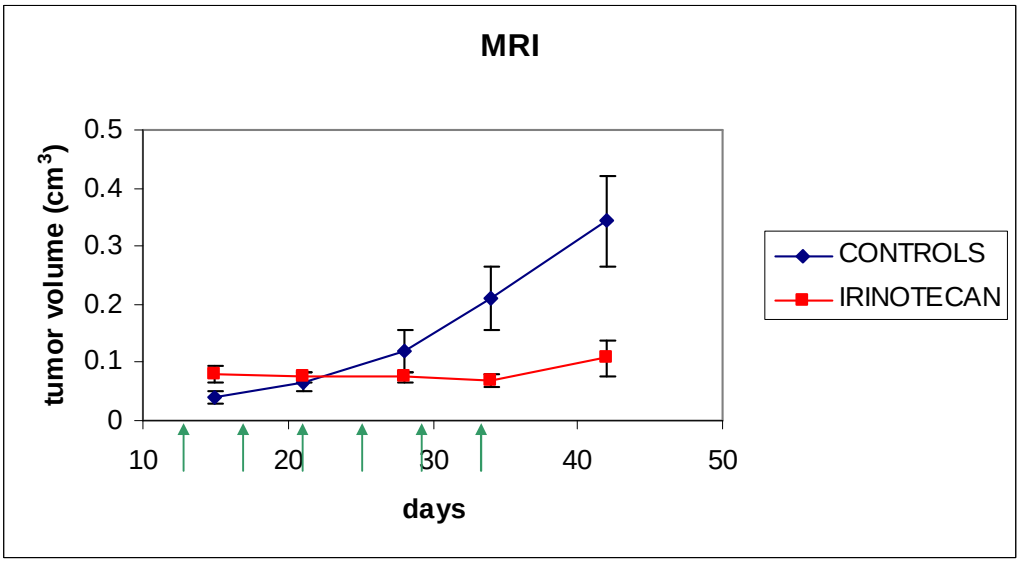

Figure 16. Tumor growth curves of control group (blue line) and treated group (red). Green arrows indicate treatment's timing.

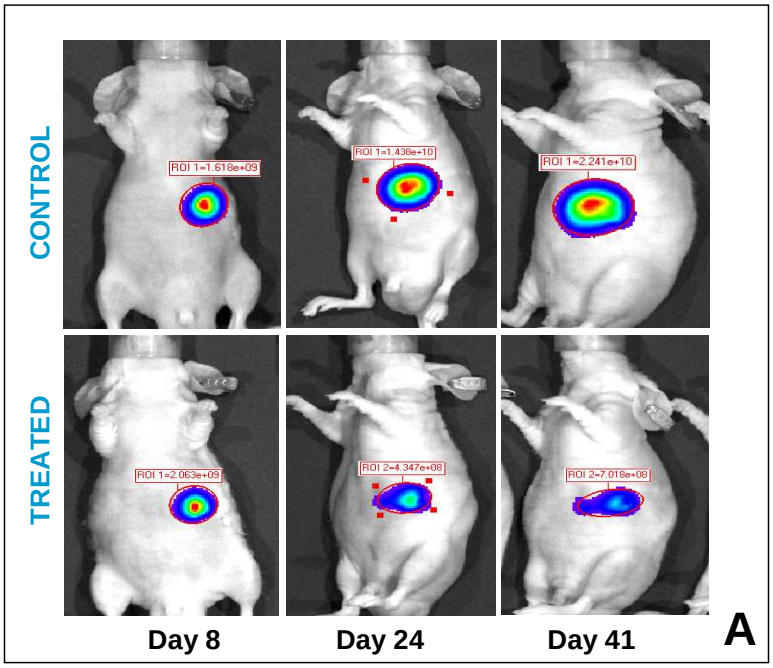

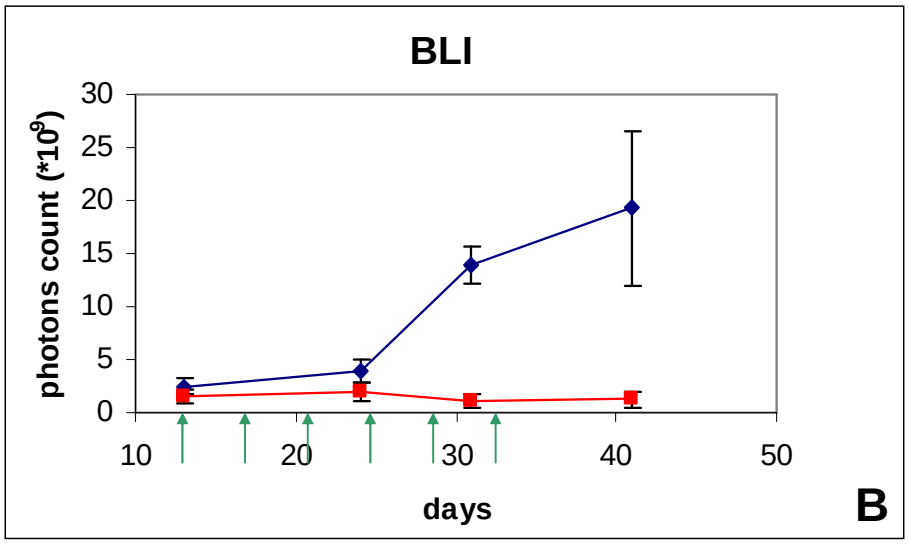

Figure 17. A) BLI images of a control (top) and of a treated mouse (bottom) are shown; B) mean values of photon emission are plotted for G1 (blue) and G2 (red). Green arrows indicate treatment's timing.

Diffusion coefficients were measured in treated tumors in comparison with controls at all tested time points, as shown in fig. 18, where ADC values are reported for each tumor. Statistically significant ($p<0.05$) higher diffusion

coefficients were detected in G2 tumors (mean ADC= 0.69 mm²/sec) compared to G1 (mean ADC= 0.84 mm²/sec), as early as day 21 (which corresponds to day 7 of treatment) when, in T2-weighted volume measurements, no significant change was yet detectable. The increase in ADC during treatment could be a result of tumor lysis, loss of cell membrane integrity, increased extracellular space, and, therefore, increase in water diffusion.

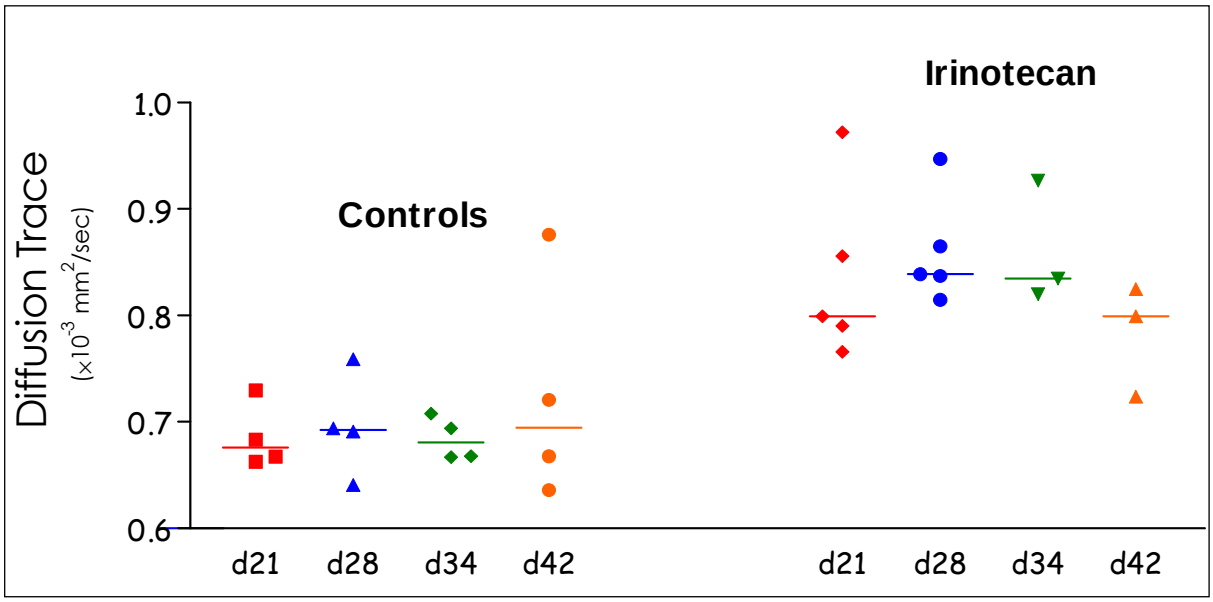

Figure 18. ADC values for e trace for each mouse during treatment: significantly higher ADC values for Irinotecan group were detected at all tested time points.

For visualization purposes, data sets were imported into Matlab environment (The MathWorks, Inc., Natick, MA). Raw data files in Bruker native format were read by a Matlab script. In particular, the axial RARE anatomical volume, the DTI-EPI series and the corresponding parametric maps of diffusion trace as derived by Paravision's analysis tool were considered. Images and parameters of interest were stored as Matlab variables.

Regions of interest encompassing the lesion were manually defined on the first b=0 image of the EPI series, and compared to the appearance of the lesion in the corresponding slice of the RARE data set to check for consistency. Voxels belonging to the ROIs were color-coded according to their value of diffusion trace, with hot colors denoting higher values and cold colors denoting lower values. Each resulting ROI map was overlaid onto the b=0 reference image, where the ROI was previously delineated (see figure 19).

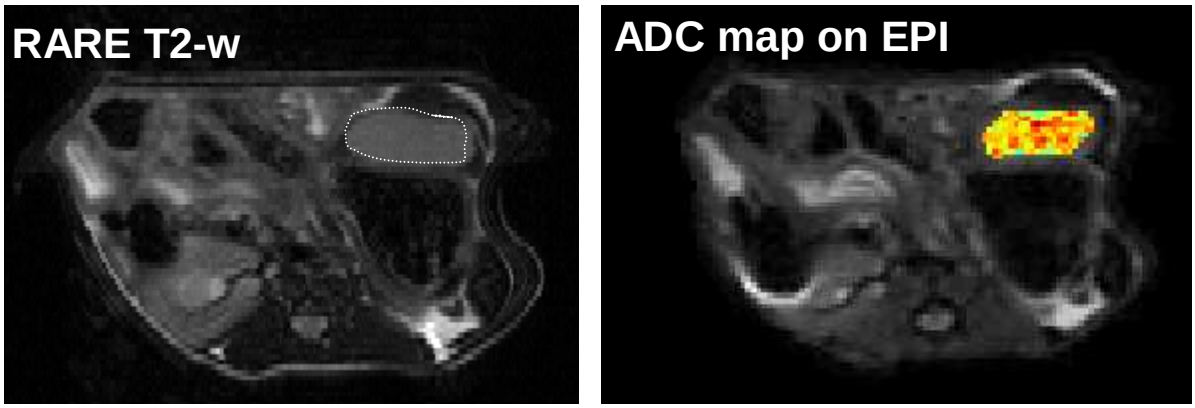

Figure 19. Regions of interest encompassing tumor on axial RARE T2-weighted images, EPI b=0 and resulting superimposed color-coded ADC map.

In figure 20 color-coded ADC maps superimposed on EPI b=0 images of a control mouse (on the left) and of a treated mouse (on the right) during treatment are shown: in the control there is a prevalence of cold colors (lower values), while in the treated mouse hot colors (higher values) are predominant, indicating tumor lysis, which could be considered as a read out of therapy efficacy.

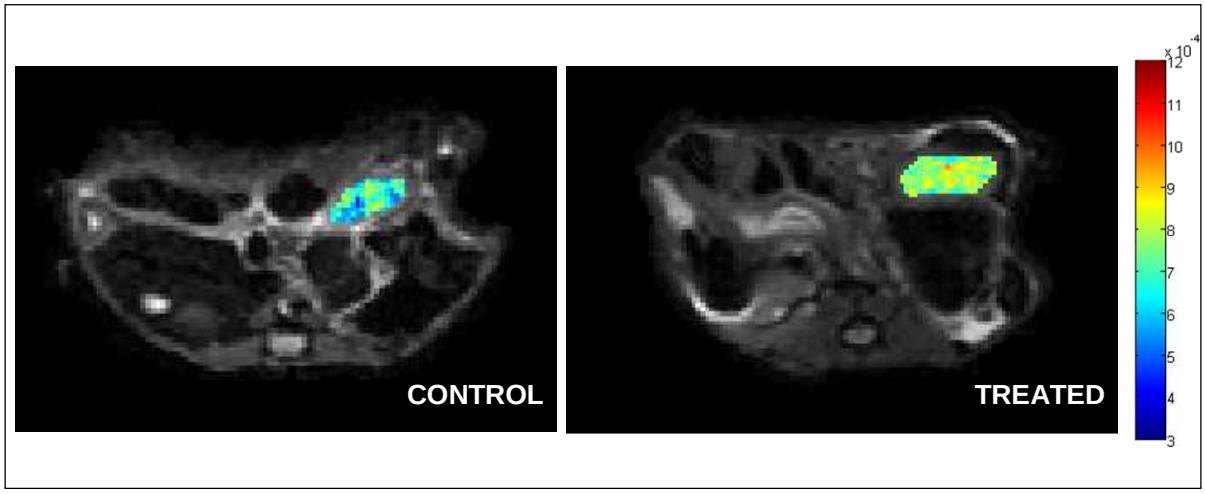

Figure 20. Color-coded ADC maps at day 7 of treatment for a control tumor (left) and Irinotecan treated tumor (right): increased ADC, depicted as hot colors, in the Irinotecan treated tumor is indicative of tumor lysis.

DISCUSSION

5 DISCUSSION

The aim of this thesis was to evaluate the use of MR imaging and BLI as tools to non-invasively localize and morphologically characterize the development and response to therapy of human pancreatic tumor cells orthotopically transplanted in nude mice. Furthermore, it was our intention to validate an advanced MR imaging tool to perform valuable pre-clinical trials in this model.

We chose to use an orthotopic xenograft tumor model that closely mimicked the clinical presentation of pancreatic cancer in patients and allowed tumors to grow in their native microenvironment. Indeed, studies of potentially therapeutic agents to non-representative preclinical models may provide an inaccurate profile of treatment efficacy and can have disappointing consequences when the agent is subsequently tested in the clinical setting. Among the two tumoral cell lines studied in our preliminary trial, the orthotopically implanted Mia-Pa-Ca-2 cell line demonstrated histological and growth patterns more suitable for an efficacy study.

In this study, we describe the combination of two complementary imaging modalities (BLI and MRI) for multimodal characterization of implants in the pancreas of immune deficient mice.

The use of luciferized cells allowed monitoring by BLI, since luciferase expression correlates with the number of tumor cells both in vitro and in vivo, and hence it is used as a reporter of cell proliferation and cell death. On the basis of these considerations, we focused on validating BLI as a non-invasive means of providing longitudinally monitoring of tumors and subsequent response to therapy. Bioluminescence served as an accurate molecular imaging surrogate for viable tumor volume detection; in fact, when tumors

were assessed longitudinally as a function of time, a linear increase in bioluminescent signal relative to tumor growth was noted. On the basis of these data, we were confidently able to use BLI for longitudinal monitoring of tumors in the same animal over time, thereby facilitating accurate assessment of normalized tumor growth over time and eliminating the need for a substantial number of animals. Indeed, the costs, inefficiency, and potential lack of accuracy associated with invasive monitoring of treatment effect are an inherent criticism of many prospective preclinical studies.

As the field of BLI continues to expand very rapidly in the preclinical experimental setting, it remains unsuitable to be translated to the clinic. This is currently unattainable owing also to the limited depth penetration of light (typically absorbed and scattered by mammalian tissues), the potential toxicity of luciferin and the potential immunogenicity of luciferases.

Similarly to other functional imaging modalities applied in the clinical practice bioluminescence resulted in poor spatial resolution, but provided an adjunctive means of identifying and targeting viable tumor when combined with MR images.

MRI on the other hand provided very detailed anatomical data regarding cell implant localization and growth.

While each of the above-described imaging techniques has its own characteristics, advantages and limitations, it is clear that a combination of these imaging techniques will provide necessary information on cell survival and function, with high resolution (given by MRI) and high sensitivity (given by BLI). Synergies derived from this multimodal approach will be useful to accurately follow cell behavior in vivo and detect changes in pathological conditions during cell therapy studies.

In this study the feasibility of obtaining good quality Diffusion Weighted (DW) images in preclinical studies outside brain has been shown, despite difficulties arising from artifacts derived from motion and artifacts and pitfalls specific to the method itself. It has been shown that DWI is a valuable, quantifiable, and early imaging biomarker of treatment response, as it was shown to correlate with traditional biomarkers of efficacy such as cell survival and kill.

The quantified apparent diffusion coefficient (ADC) has been correlated with cellular density, presence of necrosis and in the therapy setting, tumor cell apoptosis and proliferation indices [71]. A low ADC reflects impeded diffusion and can be found in highly cellular tissues or fibrosis. If there are areas of significant necrosis this results in less restriction of motion and therefore a high ADC.

Data on the expected magnitude of change in ADC indicative of response to standard therapy are becoming available for rectal, liver, lung and ovary tumors. It is likely that an increase in 20–25% after 1 week of treatment and at least 40% at later time points (3–4 weeks) of treatment will be indicative of tumor response [72]. In bone, as in soft tissue tumors an increase in ADC occurs in responding lesions but because of the contribution of low ADC values from marrow fat in response, this requires more complex analysis [73].

The ability to rapidly assess efficacy following treatment initiation provides an important opportunity to more rapidly evaluate drug dosages and combinations in preclinical studies. Moreover, because DWI is a translable technique, inclusion of DWI in phase 1 and 2 clinical trials would provide a sensitive means to detect treatment efficacy, which is especially valuable in dose escalation protocols.

There are currently no standard radiological methods for early assessment of tumor therapeutic efficacy during an interventional regimen, although several imaging approaches are under active evaluation [74-78].

DWI provides the potential to truly individualize patient treatment regimens through unbiased quantization of early treatment response. This has tremendous clinical significance as it could facilitate early identification of patients who are non-responsive to a specific intervention and thereby provide more time to try alternative therapies.

The use of diffusion MRI as a sensitive imaging biomarker, capable of detecting early cellular changes in treated tumors, which precede macroscopic volumetric response, would be a valuable and cost effective approach for managing individual patients undergoing anticancer treatment. Further impact could be seen in improvements in patients' quality of life and extension of overall survival.

REFERENCES

6 REFERENCES

1. Jemal A, Siegel R, Ward E, Hao Y, Xu J, Thun MJ. Cancer statistics. *Cancer J Clin* 2009; 59: 225-249

2. Heinemann V, Boeck S, Hinke A, Labianca R, Louvet C. Meta-analysis of randomized trials: evaluation of benefit from gemcitabine-based combination chemotherapy applied in advanced pancreatic cancer. *BMC Cancer* 2008; 8: 82

3. Sultana A, Tudur Smith C, Cunningham D, Starling N, Neoptolemos JP, Ghaneh P. Meta-analyses of chemotherapy for locally advanced and metastatic pancreatic cancer: results of secondary end points analyses. *Br J Cancer* 2008; 99: 6-13

4. Stathis A, Moore MJ. Advanced pancreatic carcinoma: current treatment and future challenges. *Nat Rev Clin Oncol* 2010; 7: 163-172

5. Bilimoria KY, Bentrem DJ, Ko CY, Stewart AK, Winchester DP, Talamonti MS. National failure to operate on early stage pancreatic cancer. *Ann Surg* 2007; 246: 173-180

6. Shrikhande SV, Kleeff J, Reiser C, Weitz J, Hinz U, Esposito I, Schmidt J, Friess H, Büchler MW. Pancreatic resection for M1 pancreatic ductal adenocarcinoma. *Ann Surg Oncol* 2007; 14: 118-127

7. Loos M, Kleeff J, Friess H, Büchler MW. Surgical treatment of pancreatic cancer. *Ann N Y Acad Sci* 2008; 1138: 169-180

8. Rivera F, López-Tarruella S, Vega-Villegas ME, Salcedo M. Treatment of advanced pancreatic cancer: from gemcitabine single agent to combinations and targeted therapy. *Cancer J Radiat Oncol Biol Phys* 2004; 60: 437-443

9. Saif MW. Adjuvant treatment of pancreatic cancer in 2009: where are we? Highlights from the 45th ASCO annual meeting. Orlando, FL, USA. May 29-June 2, 2009. *JOP* 2009; 10: 373-377

10. Fulda S. Apoptosis pathways and their therapeutic exploitation in pancreatic cancer. J *Cell Mol Med* 2009; 13: 1221-1227

11.Wong HH, Lemoine NR. Pancreatic cancer: molecular pathogenesis and new therapeutic targets. *Nat Rev Gastroenterol Hepatol* 2009; 6: 412-422

12. Conroy T, Desseigne F, Ychou M, Bouche O, Guimbaud R, Becouarn Y, et al. FOLFIRINOX versus gemcitabine for metastatic pancreatic cancer. *N Engl J Med* 2011; 364(19):1817-1825

13. Strimpakos AS, Syrigos KN, Saif MW. The molecular targets for the diagnosis and treatment of pancreatic cancer. *Gut Liver* 2010; 4(4): 433-449

14. Fogh J, Orfeo T, Tiso J, Sharkey FE, Fogh JM, Daniels WP. Twenty-three new human tumor lines established in nude mice. *Exp Cell Biol* 1980; 48: 229-39

15. Sordat BC, Ueyama Y, Fogh J. Metastasis of tumor xenografts in the nude mouse. In: Fogh J, Gilovanella BC, eds. *The nude mouse in experimental and clinical research, vol. 2. New York: Academic Press,* 1982; 95-143

16. Mohammad RM, Al-Katib A, Pettit GR, Vaitkevicius VK, Joshi U, Adsay V, Majumdar APN, Sarkar FH. An orthotopic model of human pancreatic cancer in severe combined immunodeficient mice: potential application for preclinical studies. *Clin Cancer Res* 1998; 4: 887-94

17. Wood KV. Marker proteins for gene expression. *Curr Opin Biotechnol* 1995; 6: 50-58

18. Contag CH, Spilman SD, Contag PR, et al. Visualizing gene expression in living mammals using a bioluminescent reporter. *Photochem Photobiol* 1997; 66: 523-531

19. Contag CH, Contag PR, Mullins JI, Spilman SD, Stevenson DK, Benaron DA. Photonic detection of bacterial pathogens in living hosts. *Mol Microbiol* 1995; 18: 593-603

20. Rice BW, Cable MD, Nelson MB. In vivo imaging of light-emitting probes. *J Biomed Opt* 2001; 6: 432-40

21. Contag CH, Jenkins D, Contag PR, Negrin RS. Use of reporter genes for optical measurements of neoplastic disease in vivo. *Neoplasia* 2000; 2: 41-52

22. Edinger M, Sweeney TJ, Tucker AA, Olomu AB, Negrin RS, Contag CH. Noninvasive assessment of tumor cell proliferation in animal models. *Neoplasia* 1999; 1: 303-310

23. Sweeney TJ, Mailander V, Tucker AA, et al. Visualizing the kinetics of tumor-cell clearance in living animals. *Proc Natl Acad Sci USA* 1999; 96: 12044-12049

24. Eisenhauer EA, Therasse P, Bogaerts J, et al. New response evaluation criteria in solid tumours: revised RECIST guideline (version 1.1). *Eur J Cancer* 2009; 45: 228-247

25. Wen PY, Macdonald DR, Reardon DA, et al. Updated response assessment criteria for high-grade gliomas: response assessment in neuro-oncology working group. *J Clin Oncol* 2010; 28: 1963-1972

26. Husband JE, Schwartz LH, Spencer J, et al. Evaluation of the response to treatment of solid tumour -a consensus statement of the International Cancer Imaging Society. *Br J Cancer* 2004; 90: 2256-2260

27. Benjamin RS, Choi H, Macapinlac HA, et al. We should desist using RECIST, at least in GIST. *J Clin Oncol* 2007; 25: 1760-1764

28. Le Bihan D, Breton E, Lallemand D, Aubin ML, Vignaud J, Laval-Jeantet M. Separation of diffusion and perfusion in intravoxel incoherent motion MR imaging. *Radiology* 1988; 168: 497-505

29. Thoeny HC, De Keyzer F, Vandecaveye V, et al. Effect of vascular targeting agent in rat tumor model: dynamic contrast-enhanced versus diffusion-weighted MR imaging. *Radiology* 2005; 237: 492-499

30. Guo Y, Cai YQ, Cai ZL, et al. Differentiation of clinically benign and malignant breast lesions using diffusion-weighted imaging. *J Magn Reson Imaging* 2002; 16: 172-178

31. Gauvain KM, McKinstry RC, Mukherjee P, et al. Evaluating pediatric brain tumor cellularity with diffusion-tensor imaging. *AJR* 2001; 177: 449-454

32. Sugahara T, Korogi Y, Kochi M, et al. Usefulness of diffusion-weighted MRI with echo-planar technique in the evaluation of cellularity in gliomas. *J Magn Reson Imaging* 1999; 9: 53-60

33. Lang P, Wendland MF, Saeed M, et al. Osteogenic sarcoma: noninvasive in vivo assessment of tumor necrosis with diffusion-weighted MR imaging. *Radiology* 1998; 206: 227-235

34. Stejskal EO, Tanner JE. Spin diffusion measurements: spin-echo in the presence of a time dependent field gradient. *J Chem Phys* 1965; 42: 288-292

35. Moteki T, Sekine T. Echo planar MR imaging of the liver: comparison of images with and without motion probing gradients. *J Magn Reson Imaging* 2004; 19: 82-90

36. Nasu K, Kuroki Y, Nawano S, et al. Hepatic metastases: diffusion-weighted sensitivity-encoding versus SPIO-enhanced MR imaging. *Radiology* 2006; 239: 122-130

37. Koh DM, Brown G, Riddell A, Scurr E, Collins DJ, Husband JE. Colorectal liver metastases: evaluation using MnDPDP enhanced MR imaging and breathhold single-shot echo-planar diffusion weighted MR imaging. *Eur Radiol Suppl* 2005; 15S: B144

38. Provenzale JM, Mukundan S, Barboriak DP. Diffusion-weighted and perfusion MR imaging for brain tumor characterization and assessment of treatment response. *Radiology* 2006; 239: 632-649

39. Taouli B, Vilgrain V, Dumont E, Daire JL, Fan B, Menu Y. Evaluation of liver diffusion isotropy and characterization of focal hepatic lesions with two single-shot echo-planar MR imaging sequences: prospective study in 66 patients. *Radiology* 2003; 226: 71-78

40. Kim T, Murakami T, Takahashi S, Hori M, Tsuda K, Nakamura H. Diffusion-weighted single-shot echoplanar MR imaging for liver disease. *AJR* 1999; 173: 393-398

41. Chan JH, Tsui EY, Luk SH, et al. Diffusion weighted MR imaging of the liver: distinguishing hepatic abscess from cystic or necrotic tumor. *Abdom Imaging* 2001; 26: 161-165

42. Squillaci E, Manenti G, Di Stefano F, Miano R, Strigari L, Simonetti G. Diffusion-weighted MR imaging in the evaluation of renal tumours. *J Exp Clin Cancer Res* 2004; 23: 39-45

43. Cova M, Squillaci E, Stacul F, et al. Diffusion weighted MRI in the evaluation of renal lesions: preliminary results. *Br J Radiol* 2004; 77: 851-857

44. Ries M, Jones RA, Basseau F, Moonen CT, Grenier N. Diffusion tensor MRI of the human kidney. *J Magn Reson Imaging* 2001; 14: 42-49

45. Fukuda Y, Ohashi I, Hanafusa K, et al. Anisotropic diffusion in kidney: apparent diffusion coefficient measurements for clinical use. *J Magn Reson Imaging* 2000; 11: 156-160

46. Rubesova E, Grell AS, De Maertelaer V, Metens T, Chao SL, Lemort M. Quantitative diffusion imaging in breast cancer: a clinical prospective study. *J Magn Reson Imaging* 2006; 24: 319-324

47. Sinha S, Lucas-Quesada FA, Sinha U, DeBruhl N, Bassett LW. In vivo diffusion-weighted MRI of the breast: potential for lesion characterization. *J Magn Reson Imaging* 2002; 15: 693-704

48. Dietrich O, Raya JG, Sommer J, Deimling M, Reiser MF, Baur-Melnyk A. A comparative evaluation of a RARE-based single-shot pulse sequence for diffusion-weighted MRI of musculoskeletal softtissue tumors. *Eur Radiol* 2005; 15: 772-783

49. Ichikawa T, Erturk SM, Motosugi U, et al. High-Bvalue diffusion-weighted MRI in colorectal cancer. *AJR* 2006; 187: 181-184

50. Irie H, Honda H, Kuroiwa T, et al. Measurement of the apparent diffusion coefficient in intraductal mucin-producing tumor of the pancreas by diffusion weighted echo-planar MR imaging. *Abdom Imaging* 2002; 27: 82-87

51. Moteki T, Ishizaka H. Diffusion-weighted EPI of cystic ovarian lesions: evaluation of cystic contents using apparent diffusion coefficients. *J Magn Reson Imaging* 2000; 12: 1014-1019

52. Moffat BA, Chenevert TL, Lawrence TS, et al. Functional diffusion map: a noninvasive MRI biomarker for early stratification of clinical brain tumor response. *Proc Natl Acad Sci U S A* 2005; 102: 5524-5529

53. Moffat BA, Hall DE, Stojanovska J, et al. Diffusion imaging for evaluation of tumor therapies in preclinical animal models. *MAGMA* 2004; 17: 249-259

54. Thoeny HC, De Keyzer F, Chen F, et al. Diffusion weighted MR imaging in monitoring the effect of a vascular targeting agent on rhabdomyosarcoma in rats. *Radiology* 2005; 234: 756-764

55. Chen CY, Li CW, Kuo YT, et al. Early response of hepatocellular carcinoma to transcatheter arterial chemoembolization: choline levels and MR diffusion constants-initial experience. *Radiology* 2006; 239: 448-456

56. Chenevert TL, McKeever PE, Ross BD. Monitoring early response of experimental brain tumors to therapy using diffusion magnetic resonance imaging. *Clin Cancer Res* 1997; 3: 1457-1466

57. Einarsdottir H, Karlsson M, Wejde J, Bauer HC. Diffusion weighted MRI of soft tissue tumours. *Eur Radiol* 2004; 14: 959-963

58. Koh DM, Scurr E, Collins DJ, et al. Predicting response of colorectal hepatic metastases: the value of pre-treatment apparent diffusion coefficients. *AJR* April 2007; 188: 1001-1008

59. Yoshikawa T, Kawamitsu H, Mitchell DG, et al. ADC measurement of abdominal organs and lesions using parallel imagingtechnique. *AJR Am J Roentgenol* 2006;187: 1521-1530

60. Matsuki M, Inada Y, Nakai G, et al. Diffusion-weighed MR imaging of pancreatic carcinoma. *Abdom Imaging* 2007; 32: 481-483

61. Irie H, Honda H, Kuroiwa T, et al. Measurement of the apparent diffusion coefficient in intraductal mucin-producing tumor of the pancreas by diffusion-weighted echo-planar MR imaging. *Abdom Imaging* 2002; 27: 82-87

62. Fattahi R, Balci NC, Perman WH, et al. Pancreatic diffusion weighted imaging (DWI): comparison between mass-forming focal pancreatitis (FP),

pancreatic cancer (PC), and normal pancreas. *J Magn Reson Imaging* 2009; 29: 350-356

63. Lee SS, Byun JH, Park BJ, et al. Quantitative analysis of diffusion-weighted magnetic resonance imaging of the pancreas: usefulness in characterizing solid pancreatic masses. J *Magn Reson Imaging* 2008; 28: 928-936

64. Muraoka N, Uematsu H, Kimura H, et al. Apparent diffusion coefficient in pancreatic cancer: characterization and histopathological correlations. *J Magn Reson Imaging* 2008; 27: 1302-1308

65. Inan N, Arslan A, Akansel G, Anik Y, Demirci A. Diffusion weighted imaging in the differential diagnosis of cystic lesions of the pancreas. *AJR Am J Roentgenol* 2008; 191: 1115-1121

66. He Z, Eveloch J, Mohammad RM et al. Magnetic resonance imaging to measure therapeutic response using an orthotopic model of human pancreatic cancer. *Pancreas* 2000; 21: 69-76

67. Grimm J, Potthast A, Wunder A et al. Magnetic resonance Imaging of the pancreas and pancreatic tumors in a mouse orthotopic model of human cancer. *Int. J Cancer* 2003; 106: 806-811

68. Samkoe KS, Chen A, Rizvi I et al. Imaging tumor variation in response to photodynamic therapy in pancreatic cancer xenograft models. *Int J Radiation oncology Biol. Phys* 2010; 76: 251-259

69. Herneth AM, Guccione S, Bednarski M. Apparent Diffusion Coefficient: a quantitative parameter for in vivo tumor characterization. *Eur. J. Radiol*. 2003; 45: 208-213

70. Kim H, Morgan D, Buchsbaum D et al. Early therapy evaluation of combined anti-death receptor 5 antibody and gemcitabine in orthotopic pancreatic tumor xenografts by diffusion-weighted magnetic resonance imaging. *Cancer Res* 2008; 68: 8369-8376

71. Padhani AR, Liu G, Koh DM, Chenevert TL, Thoeny HC, Takahara T, Dzik-Jurasz A, Ross BD, Van Cauteren M, Collins D, Hammoud DA, Rustin GJ, Taouli B, Choyke PL. Diffusion-weighted magnetic resonance imaging as

a cancer biomarker: consensus and recommendations. *Neoplasia* 2009; 11(2): 102-125

72. Sun YS, Cui Y, Tang L, Qi LP, Wang N, Zhang XY, Cao K, Zhang XP. Early evaluation of cancer response by a new functional biomarker: apparent diffusion coefficient. *Am J Roentgenol* 2011; 197(1): W23-W29

73. Messiou C, Collins DJ, Giles S, de Bono JS, Bianchini D, de Souza NM. Assessing response in bone metastases in prostate cancer with diffusion weighted MRI. *Eur Radiol* 2011; 21: 2169-2177

74. Blankenberg F, Mari C, Strauss HW. Imaging cell death in vivo. *Q. J. Nucl. Med*. 2003; 47: 337-348

75. Spence AM, Mankoff DA, Muzi M. Positron emission tomography imaging of brain tumors. *Neuroimaging Clin. N. Am.* 2003; 13: 717-739

76. Van de Wiele C, Lahorte C, Oyen W, Boerman O, Goethals I, Slegers G, Dierckx RA. Nuclear medicine imaging to predict response to radiotherapy: a review. *Int. J. Radiat. Oncol. Biol. Phys.* 2003; 55: 5-15

77. Belhocine T, Steinmetz N, Green A, Rigo P. In Vivo Imaging of Chemotherapy-Induced Apoptosis in Human Cancers. *Ann. N.Y. Acad. Sci*. 2003; 1010: 525-529

78. Nelson, S. J. & Cha, S. Imaging glioblastoma multiforme. *Cancer J.* 2003; 9: 134-145

APPENDICES

7 APPENDIX 1

Principles of Nuclear Magnetic Resonance

Nuclear Magnetic Resonance (NMR) deals with the interaction between an oscillating magnetic field and the net magnetization of a sample, which originates from its constituent nuclei in the presence of a static magnetic field. The nuclei at the centre of atoms are electrically charged for the presence of protons. In addition, many atomic nuclei (isotopes or nuclides) possess an angular momentum or spin I, which is caused by the rotation of nucleus about its axis. In principle, the nuclear spin follows the rules of quantum mechanics. A rotating charge (circular current) induces a magnetic dipole (μ); thus, all atomic nuclei with spin I behave as tiny compass needles. As long as no external magnetic fields exist these "compass needles" are statistically oriented in all possible spatial directions. If we subject a substance to a magnetic field (B0), the magnetic dipoles strive to align themselves along the direction of the magnetic field, and the magnetization precesses along a conical path around the B0 field direction. According to quantum mechanics, an angular momentum can have only a restricted number of alignments with respect to the magnetic field. Hence, the angular momentum of, for example, the hydrogen nucleus (proton, 1H), which has spin I = 1/2, can have only two (2I + 1) possible stable orientations relative to the magnetic field B0: one parallel to the magnetic field, the other anti-parallel to it. The two spin states differ in their energy such that the probability of finding a spin in a certain state is not uniform. A parallel orientation obviously means less energy than an antiparallel direction. The difference in energy ΔE is proportional to the field strength B0: this means that doubling the field strength entails a

doubling of energy difference. There is in addition a temperature effect: at absolute zero all the nuclear spins are aligned along the field direction, whereas at room temperature the thermal energy works against alignment, i.e. temperature interferes with an ordered arrangement. As a result, the two energy levels are not equally populated and there is a slight predominance of vectors in the parallel configuration, according to the Boltzmann‟s law distribution. At a typical magnetic field strength at room temperature and in thermal equilibrium, for every one million nuclei at the higher energy level one million and six nuclei would exist at the lower energy level. Consequently, a macroscopic magnetization Mz in the magnetic field results as the sum of all microscopic nuclear magnetic dipole moments and this magnetization can be detected. The net magnetization lies along the axis of the main magnetic field, in general defined as z-axis, and is named “Longitudinal Magnetization”.

The nuclei of atoms placed in a magnetic field are not exactly aligned along the direction of the lines of force of the field: the magnetic axis of each nucleus tends to be disposed in an oscillating way along the vector of field itself, as with the needle of the compass. This oscillation combines with the motion of spin, giving rise to a complex movement of rotation on a conical surface having its axis along the direction of stable magnetic field. This movement is called precession of the nuclei and is similar to the motion of a gyroscope that oscillates on its axis of rotation due to the gravity field of the earth. The speed of precession is proportional to the magnetic field strength and is different for each atom. The precession rate is called Larmor frequency and, for hydrogen nucleus, is in the range of radiofrequencies.

If we irradiate the sample with radio waves in the MHz frequency range, the proton will absorb the energy and be promoted to the less favourable higher

energy state. The precession rate of all nuclei is in the same position of conic surface. This energy absorption is called resonance, because the frequency of the applied radiation and the precession cohincide or resonate.

The resulting effect of the nucleus in phase concordance is the formation of a new magnetization vector along the x-y plane, perpendicular to B0 vector, named Transverse Magnetization.

When radiofrequency pulse is removed, nuclei start loosing their stored energy, generating radiofrequency waves that can be detected. During this phenomenon, the net magnetization from the xy plane will rotate back until is again aligned with B0. At the same time all spins will spread out and loose coherence with each other and the x-y component of the magnetization will gradually disappear.

The recovery of longitudinal magnetization occurs with a time constant T1, referred to as T1 o spin lattice relaxation time: the energy is just handed over to their surroundings, the so-called lattice. The gradual loss of transversal magnetization occurs with a time constant T2, referred to as T2 or spin-spin relaxation time. Each nucleus in fact is influenced by the small magnetic fields from neighbouring nuclei, which are somehow characteristics for a tissue. Since the nuclear spin relaxation process depends on the existence of molecular motions to generate a randomly varying magnetic field, from the relaxation rates we can get valuable information about these motions and therefore about the type of tissue.

To obtain measures "weighed" in a selective manner according to the T1 time (recovery of longitudinal magnetisation) or T2 (loss of transversal magnetization), it is essential to use specific sequences of nuclear excitation and collection of signals. It will be possible to have images with desired

weighting varying the types of acquisition and/ or regulatory factors of the sequences.

The most common sequence is the Spin-Echo (SE) sequence, which allows to get values weighed in T2 without the interference of the dishomogeneities of the magnetic field. This sequence is also highly flexible and, by varying some acquisition parameters, it is possible to obtain also weighted measures in T1 and proton density. The transverse magnetization is sensitive to the intrinsic dishomogeneities, which are inevitably present in any magnetic field. They would lead to a false interpretation of results, because they determine an apparent more rapid decay of T2, due to the spontaneous dephasing of nuclei of atoms excited. To eliminate this problem, the rephasing signal of nuclear spin after an RT pulse at 180° to the magnetic field is recorded with the Spin-Echo sequence. Each SE sequence is composed of an initial pulse at 90° to bring the magnetization on the transverse plane. If the signal is measured at this time, a FID signal (Free Induction Decay), the spontaneous fall of the magnetization in the absence of other pulses, can be collected. Then a pulse at 180° is applied. Since the magnetization vector is currently on the transverse plane, this impulse has the effect of "flip" the orientation of the spin direction. In this way, after a time equal to twice the time elapsed between the pulse at 90° and 180°, the precession of the nuclei back into phase and the transverse magnetization takes a maximum value that is measured by the instrument.

If a whole series of 180° pulses is applied, it results in a continuous rephasing of the nuclei in the opposite direction, with production of a succession of spin-echoes. Because no energy is added at the system, each registration of signal T2 is worth less and less, permitting the record of the fall of the transverse magnetization. This sequence, comprising one 90° pulse followed by a series of 180° pulses, is termed a "Carr-Purcell sequence".

The SE sequence is characterized by three fundamental parameters that must be programmed by the operator, and whose values determine the characteristics of the final images. First, the repetition time of pulse at 180°, namely number of points, that represents a discretisation of the total time of measurement. This is the parameter which decides the length of the sequence and the start of a subsequent phase of acquisition. Secondly, the interval between pulse at 90° to 180° determines the time to echo (π), which is equal to twice this value, since half the time is spent to allow the de-phasing of the precession of protons. The other half, just the same, spends between 180° pulse and collection of eco of spin resulting by rephasing. Finally, the presence of a possible repetition pulse at 180° within a given sequence is determined by the echo number. This repetition allows the collection of late echoes, useful for evaluating the signal deriving from sample test characterized by long T2.

Principles of Magnetic Resonance Imaging (MRI)

The Magnetic Resonance Imaging (MRI) is an image generating technique based on NMR. Hydrogen is the most commonly observed nucleus in MRI, because of its favourable magnetic properties and its abundance. 1H-MR images reflect the density of Hydrogen, main component in tissues as water or fat. MRI signal intensity reflects the number of MR-visible protons in a unit volume of tissue. In other words it reflects the density of mobile Hydrogen nuclei influenced by their chemical environment, which causes magnetic relaxation times T1 and T2.

The main components of an MR imaging system are :

- the magnet, that generates the magnetic field and polarizes the sample;

- the magnetic field gradients, for spatial reconstruction and localization of signal;
- the radiofrequency coils to transmit and/or receive the MR imaging signal;
- one or more computer and associated signal processing equipment.

The Magnet

The magnet is the largest and most expensive component of the scanner. Its strength is measured in Tesla (T). Clinical magnets generally have a field strength in the range 0.1-3.0 T, with research systems available up to 9.4 T for human use and 21 T for animal systems. The homogeneity of the basic magnetic field over the examination volume should be as high as possible, to ensure low image distortion and high signal homogeneity and achieve good image quality. Also, the homogenous examination volume should be as large as possible. A cylindrical main magnet with the homogeneous volume centred on the central axis fulfills all these requirements and, therefore, represents the most frequent magnet designed today. In general, the magnet is based on the use of superconducting electromagnet. When a Niobium-Titanium or Niobium-Tin alloy is cooled by liquid Helium to −269°C it becomes a superconductor, with low resistance to the flow of electrical current and extremely high field strengths, with very high stability. Helium cooled superconducting magnets are the most common type found in MRI scanners today. Most superconducting magnets have their coils of superconductive wire immersed in liquid Helium, inside a vessel called a cryostat. Despite thermal insulation, ambient heat induces the Helium to slowly boil off. Such magnets, therefore, require regular topping-up with liquid Helium. Generally

a cryocooler, also known as coldhead, is used to condense some Helium vapour back into the liquid Helium bath. Several manufacturers now offer 'cryogenless' scanners where, instead of being immersed in liquid Helium, the magnet wire is cooled directly by a cryocooler.

When a sample is placed into the scanner, it creates inhomogeneities in the field. This causes regions without signal and spatial distortion in the acquired images. To restore the field homogeneity, a set of shim coils are included in the scanner. These are resistive coils, usually at room temperature, capable to produce secondary magnetic fields which correct inhomogeneities and errors in the magnetic field strength. This process of “shimming” is usually automated.

The Gradient System

The magnetic field gradients give rise to linear variations of magnetic field strength. In fact, gradient coils are used to spatially encode the positions of protons by varying the magnetic field linearly across the imaging volume. In order to produce an image, 3 gradients in 3 orthogonal orientations are used: one gradient is used to “locate” the level of each plane and is known as “slice gradient”. The other two gradients are used to locate points within each plane and are called “frequency” and “phase encoding” gradients.

Gradient coils are usually resistive electromagnets powered by sophisticated amplifiers which permit rapid and precise adjustments of field strength and direction.

Scan speed depends on the gradient system performance. An optimal system must be able to cover large examination volume in the shortest possible time.

In general, the gradient system requirements can be best met with a cylindrical design that fits magnet geometry.

The Radiofrequency System

The radiofrequency (RF) system consists of a RF transmit coil inside the magnet, for selective RF spins excitation and a RF receiver coil system, for picking up the weak RF signal resulting from excited nuclei.

Radiofrequency coils can be constructed with a variety of geometries and they are increasingly built for specific applications; however, large cylindrical volume transmit RF coils with a conductor geometry similar to a birdcage are typically used.

Image Formation

The radiofrequency signal picked up by the receiver at the end of an acquisition does not have an intrinsic spatial information because it is unable to discriminate signals deriving from different points of the sample. Thus it cannot be used to reconstruct an image. The passage between raw signal and the image formation is based on a process of spatial codification, with attribution of a specific frequency and resonance phase for each point of the space, thanks to the application of the gradients.

Each different point of the examined space, identified through a frequency and phase codification, is assigned a numeric value of intensity that is translated in a different intensity of grey scale on the image.

Spin Echo and Gradient Echo sequences, fast imaging and ultra fast imaging.